NKCC1 modulates microglial phenotype, cerebral inflammatory responses and brain injury in a cell-autonomous manner

Krisztina Tóth[1,2], Nikolett Lénárt[1], Péter Berki[2,7], Rebeka Fekete[1], Eszter Szabadits[1], Balázs Pósfai[1,2], Csaba Cserép[1], Ahmad Alatshan[3,4], Szilvia Benkő[3, 4], Dániel Kiss[8], Christian A. Hübner[5], Attila Gulyás[7], Kai Kaila[6], Zsuzsanna Környei[1] and Ádám Dénes[1,]*

[1] Momentum Laboratory of Neuroimmunology, Institute of Experimental Medicine, Budapest, H-1083 Hungary

[2] János Szentágothai Doctoral School of Neuroscience, Semmelweis University, Budapest, H-1083 Hungary

[3] Department of Physiology, Faculty of Medicine, University of Debrecen, Debrecen, H-4012 Hungary

[4] Doctoral School of Molecular Cellular and Immune Biology, Faculty of Medicine, University of Debrecen, Debrecen, H-4012 Hungary

[5] University Hospital Jena of Friedrich Schiller University, Jena, 07737 Germany

[6] Molecular and Integrative Biosciences and Neuroscience Center (HiLIFE), University of Helsinki, Helsinki, 00014 Finland

[7] Laboratory of Cerebral Cortex Research, Institute of Experimental Medicine, Budapest, H-1083 Hungary

[8] John von Neumann Faculty of Informatics, Óbuda University, H-1034 Hungary

[*] Correspondence: denes.adam@koki.hu

Abstract

The NKCC1 ion transporter contributes to the pathophysiology of common neurological disorders, but its function in microglia, the main inflammatory cells of the brain, has remained unclear to date. Therefore, we generated a novel transgenic mouse line in which microglial NKCC1 was deleted. We show that microglial NKCC1 shapes both baseline and reactive microglia morphology, process recruitment to the site of injury, and adaptation to osmotic stress in a cell-autonomous manner via regulating membrane potential and chloride fluxes. In addition, microglial NKCC1 deficiency results in increased expression of the D subunit of volume regulated anion channel (VRAC), NLRP3 inflammasome priming and production of interleukin-1β (IL-1β), rendering microglia prone to exaggerated inflammatory responses. In line with this, central (intracortical) administration of the NKCC1 blocker, bumetanide, potentiated intracortical lipopolysaccharide (LPS)-induced cytokine levels, whereas systemic bumetanide application decreased inflammation in the brain. Microglial NKCC1 KO animals exposed to experimental stroke showed significantly increased brain injury, inflammation, cerebral edema and worse neurological outcome. Thus, NKCC1 emerges as an important player in controlling microglial ion homeostasis and inflammatory responses through which microglia modulate brain injury. The contribution of microglia to central NKCC1 actions is likely to be relevant for common neurological disorders.

38 ## Introduction

39 Members of the plasmalemmal cation-chloride cotransporter (CCC) family, such as the neuron-specific
40 K^+/Cl^- extruder, KCC2, and the ubiquitously expressed Na^+-K^+-$2Cl^-$ cotransporter, NKCC1 (coded by the
41 *Slc12a2* gene), have received a steeply increasing amount of attention in research on CNS diseases,
42 ranging from neuropsychiatric diseases to epilepsy, stroke and dementia [1–6]. Notably, there's an
43 abundance of studies, which have shown that the mRNA and protein expression levels as well as the
44 functionality of NKCC1 are enhanced in injured and post-traumatic neurons [7,8]. This, in turn, has
45 raised the obvious possibility that assuming a pathophysiological role for NKCC1, therapeutic actions
46 might be achieved by pharmacological inhibition of this transporter. Indeed, data in a number of
47 experimental studies based on systemic application of the selective NKCC1 blocker, the loop diuretic
48 bumetanide, have suggested that this drug has therapeutic actions in diverse neuropathological
49 conditions. These include neonatal seizures, temporal lobe epilepsy, autism spectrum disorders,
50 schizophrenia, and brain edema after traumatic or hypoxic/ischaemic injury [1–4,7–12]. In most of
51 these studies, bumetanide has been suggested to exert its therapeutic effects by acting directly on
52 NKCC1 expressed in central neurons.

53 While bumetanide is routinely used to block neuronal NKCC1 in experiments performed *in vitro*
54 [3,8,12], the view that the drug might have direct effects on central neurons *in vivo* has raised
55 numerous questions. First, the poor pharmacokinetic properties of bumetanide, including a low
56 permeability to active coupled extrusion across the blood-brain barrier (BBB) would imply that the
57 drug does not reach pharmacologically relevant concentrations in the brain parenchyma, a prediction
58 that has been experimentally verified [10,13,14]. Another important point in the present context is
59 that NKCC1 is expressed within the immature and mature CNS mainly in non-neuronal cell types [15],
60 such as oligodendrocytes and their precursors [16,17], ependymal cells and astrocytes [18–21]. Thus,
61 even if applied directly into brain tissue, bumetanide or any other NKCC1 blockers would be expected
62 to inhibit this ion transporter in a wide variety of cell types.

63 Interestingly, common neurological disorders including those with altered NKCC1 activity [6,7,22]
64 display broad neuroinflammatory changes. While the impact of NKCC1 function on inflammatory
65 cytokine production has not been widely studied, emerging evidence indicates upregulated NKCC1
66 expression in response to inflammatory stimuli (LPS, IL-1β, TNF-α) [23–26]. Notably, while microglia
67 are the main inflammatory cell type in the CNS, there is no information about the functional role of
68 NKCC1 in microglia and whether microglial NKCC1 could provide a significant contribution to central
69 NKCC1 actions under inflammatory conditions or after brain injury.

70 In the healthy brain, microglia regulate neuronal activity and responses, whereas altered microglial
71 activity is linked with the pathophysiology of most common brain disorders, such as
72 neurodegenerative and psychiatric diseases, stroke and epilepsy [27–33]. Extracellular accumulation
73 of potassium is related to diverse neuropathological alterations [32,34], and the contribution of
74 microglial potassium channels and transporters to microglial activity is widely recognized. These
75 include membrane-expressed potassium channels (Kv1.3, THIK-1, Kir2.1) that regulate microglial
76 motility, immune surveillance and cytokine release, among others [35,36]. Moreover, changes in
77 intracellular potassium and chloride levels are associated with inflammasome activation contributing
78 to the regulation of IL-1β release [37–39]. Interestingly, recent transcriptomic data verified high-level
79 NKCC1 expression in microglia [21,40]. However, currently no experimental data are available on the
80 function of microglial NKCC1 under physiological and pathological conditions. To this end, we studied
81 whether central and systemic NKCC1 blockade impact on central inflammatory changes differently and
82 tested the hypothesis that NKCC1 is involved in the regulation of microglial inflammatory mediator
83 production, neuroinflammation and brain injury.

84

85 ## Results

86

87 **Systemic and central blockade of NKCC1 regulate LPS-induced inflammatory cytokine production in**
88 **the brain in an opposite manner**

89 To investigate whether *systemic blockade of NKCC1 actions* by bumetanide could alter inflammatory
90 responses in the CNS, we injected mice either intraperitoneally or intracortically with bacterial
91 lipopolysaccharide (LPS), while NKCC1 actions were blocked by systemic (intraperitoneal; ip.)
92 bumetanide administration (Figure 1A). As expected, LPS administration by ip. injection triggered
93 marked inflammation in the spleen and the liver (Supplementary Figure 1A), but caused low cytokine
94 production in cortical brain tissues, which was not influenced by ip. bumetanide treatment (Figure 1A).
95 However, bumetanide resulted in a small, but significant increase in LPS-induced IL-1β production in
96 the spleen (Supplementary Figure 1A). In contrast, intracortical LPS administration triggered a robust
97 inflammatory response in the brain as seen earlier [41], which was reduced by ip. bumetanide
98 treatment. This was demonstrated by lower G-CSF, KC, IL-1β, and IL-1α levels in the brain (by 39.8%,
99 43%, 54.6% and 41%, respectively), while systemic cytokine levels were not altered (Supplementary
100 Figure 1A).

101 To compare the effects of systemic versus central NKCC1 blockade by bumetanide, we next
102 investigated the impact of *central (intracortical) bumetanide administration* on LPS-induced cytokine
103 responses, by co-injecting bumetanide with LPS (Figure 1B) into the cerebral cortex. As expected,
104 intracortical LPS without bumetanide resulted in a 20-50-fold increase in inflammatory
105 cytokines/chemokines in the cerebral cortex compared to vehicle. Surprisingly, on top of this,
106 bumetanide markedly potentiated LPS-induced G-CSF, KC, IL-1β and IL-1α levels in the brain (by 86.1%,
107 31.2%, 82.5% and 72.4%, respectively), in sharp contrast with the effects of ip. bumetanide treatment
108 (Figure 1A). Intracortical bumetanide had no effect on systemic cytokine levels (Supplementary Figure
109 1B).

110 We next tested whether the effects of central bumetanide administration on increasing cytokine
111 production might be explained by altered LPS-induced recruitment of leukocytes. However, while flow
112 cytometry revealed increased number of infiltrating $CD45^{high}$ leukocytes, in particular $CD11b^{+}$ $Ly6G^{high}$
113 granulocytes, and $CD11b^{+}$ $Ly6G^{-}$ $Ly6C^{high}$ monocytes in response to central LPS injection compared to
114 vehicle administration (Figure 1C), this was not altered by central bumetanide. The number of $CD45^{int}$
115 $CD11b^{+}$ microglia was not affected either (Figure 1C), indicating that the increased LPS-induced
116 cytokine production observed upon central bumetanide treatment is not due to altered inflammatory
117 cell numbers in the cerebral cortex. Unbiased densitometric analysis revealed that GFAP and AQP4
118 immunopositivity 24 hours after intracortical LPS injection were not altered by central bumetanide
119 treatment (Supplementary Figure 2), suggesting that while bumetanide may also act on astroglial
120 NKCC1 [18–20], marked changes in astrocyte phenotypes or perivascular astrocyte endfeet are unlikely
121 to explain the effect of bumetanide on central inflammatory responses in the present study.

122 Microglia are the primary source of inflammatory cytokines in a number of neuropathologies, and IL-
123 1β, also produced by microglia, is a key proinflammatory cytokine regulating the brain's cytokine
124 network [42,43]. To investigate the cellular source of IL-1β in this experimental model, we injected LPS
125 intracortically into $Cx3CR1^{+/GFP}$ (microglia reporter) mice. Multi-label immunostainings confirmed that
126 Cx3CR1-GFP microglia coexpressing P2Y12R and CD45 displayed cytoplasmic IL-1α and IL-1β
127 production (Figure 1D). These findings collectively suggested that microglia are likely to be major
128 mediators of central bumetanide actions under inflammatory conditions. Supporting this, central LPS
129 administration resulted in a significant decrease of NKCC1 (encoded by *Slc12a2*) mRNA levels, along
130 with a decline of P2Y12R mRNA, a key purinergic receptor reportedly associated with homeostatic
131 microglial actions, microglial activation and response to injury (Figure 1E) [31,44–46].

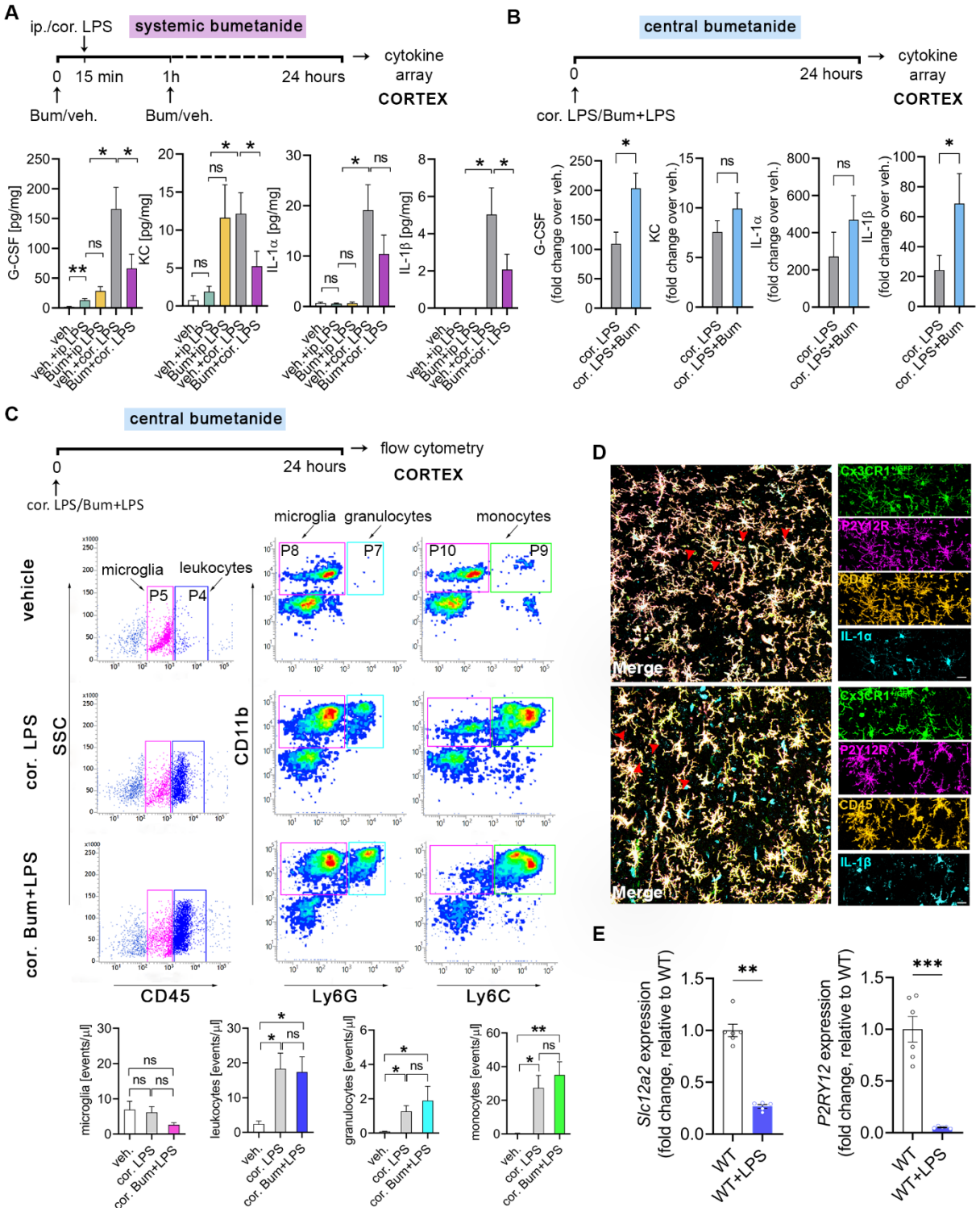

Figure 1. Systemic and central (intracortical) blockade of NKCC1 regulate LPS-induced inflammatory cytokine production in the brain in an opposite manner. A: Mice were subjected to either intraperitoneal (ip.) or intracortical (cor.) LPS injections, while NKCC1 was blocked by ip. bumetanide (Bum) administration. Central LPS injection triggers high cytokine (G-CSF, IL-1α, IL-1β) and chemokine (KC) responses in the brain compared to ip. LPS injection, which is blocked by ip. Bum administration. **B:** Central NKCC1 inhibition by intracortical Bum administration significantly increases GCSF and IL-1β levels. See also Supplementary Figure 1 for effects of systemic vs. central blockade of NKCC1 on LPS-induced cytokine responses in the periphery. **C:** Flow cytometric dot plots show that cortical

141 administration of Bum does not affect the number of microglia ($CD45^{int}$/P5 gate), and recruitment of
142 leukocytes ($CD45^{high}$/P4 gate), including monocytes ($CD11b^{+}$, $Ly6C^{high}$ /P9 gate), and granulocytes
143 ($CD11b^{+}$, $Ly6G^{high}$/P7 gate) upon central LPS injection. **D:** The main source of IL-1α and IL-1β in the brain
144 are microglia cells. Confocal images of $Cx3CR1^{+/GFP}$ brain slices show IL-1α-CD45-P2Y12R (above, red
145 arrowheads) and IL-1β-CD45-P2Y12R (below, red arrowheads) labelled cells after cortical LPS injection-
146 induced inflammation. All data are expressed as mean±SEM. **E**: NKCC1 (encoded by *Slc12a2*) and
147 P2Y12R gene expression is downregulated in microglia isolated from adult mice 24 hours after cisterna
148 magna LPS application. **A:** One-way ANOVA followed by Tukey's multiple comparison test; *p<0.05;
149 N=6/group; **B:** Unpaired t-test; *p<0.05; N=9/group; Data were pooled from two independent studies.
150 **C:** One-way ANOVA followed by Tukey's multiple comparison test; *p<0.05; N=4/group. **D:** Scale: 25
151 µm; **E:** Unpaired t-test; **p<0.01, ***p<0.001; N (WT)=6, N (KO)=5; Abbreviations: veh.: vehicle; ip:
152 intraperitoneal; cor.: cortical; Bum: bumetanide; ns: not significant

153
154
155
156 **Deletion of microglial NKCC1 markedly impacts on baseline cell morphology and alters**
157 **transformation to reactive microglia**

158 Available RNA-seq data demonstrate that the *Slc12a2* gene is expressed by microglia [21,40]. In line
159 with this, our qPCR data revealed that mRNA levels of NKCC1 in microglial cells isolated from newborn
160 (1.052±0.054) or adult (0.89±0.098) C57BL/6J mice are comparable to those in neural progenitors
161 derived from embryonic brains (1.30±0.05; Figure 2A). However, NKCC1 mRNA expression markedly
162 decreased when cells were grown in culture for 10 days (Figure 2A), making it difficult to study NKCC1
163 function in microglia using *in vitro* techniques.

164 To study the functional role of NKCC1 in microglia *in vivo*, we generated a novel transgenic mouse line
165 in which microglial NKCC1 was deleted (Figure 2B). *Slc12a2* expression in isolated microglia derived
166 from tamoxifen-inducible microglial NKCC1 KO mice was markedly reduced in comparison with wild
167 type littermates (WT: 1.46±0.11, KO: 0.50±0.016; Figure 2C) as assessed by qPCR. Reduced NKCC1
168 protein expression was also confirmed by unbiased fluorescent density measurements after systematic
169 random sampling of a great number of individual microglial cells from Iba1/NKCC1 stained slices. In
170 fact, a discrete NKCC1-labeling was seen in the plasma membrane of microglial cells in WT mice, which
171 was absent in microglial NKCC1 KO mice (Figure 2D-E).

Microglia are known to respond to physiological and pathological challenges with fast morphological transformation [47], while the role of NKCC1 in cell volume regulation has been highlighted in previous studies concerning other cell types [48,49]. To study the role of NKCC1 in microglial cell shape, we performed automated morphological analysis using perfusion-fixed brain sections obtained from WT and microglial NKCC1 KO mice (Figure 2F-G). First, we aimed to test whether microglial NKCC1 deficiency has any impact on baseline cell morphology. Our data revealed that NKCC1-deficient microglia displayed a 23.8% higher cell surface, 19% higher branch volume, and 33.5% more branches compared to WT cells (Figure 2F-G), while we observed no changes in the cell body volume of KO versus WT microglia (Figure 2G). According to these data, microglial NKCC1 is likely to be involved in shaping baseline cell morphology.

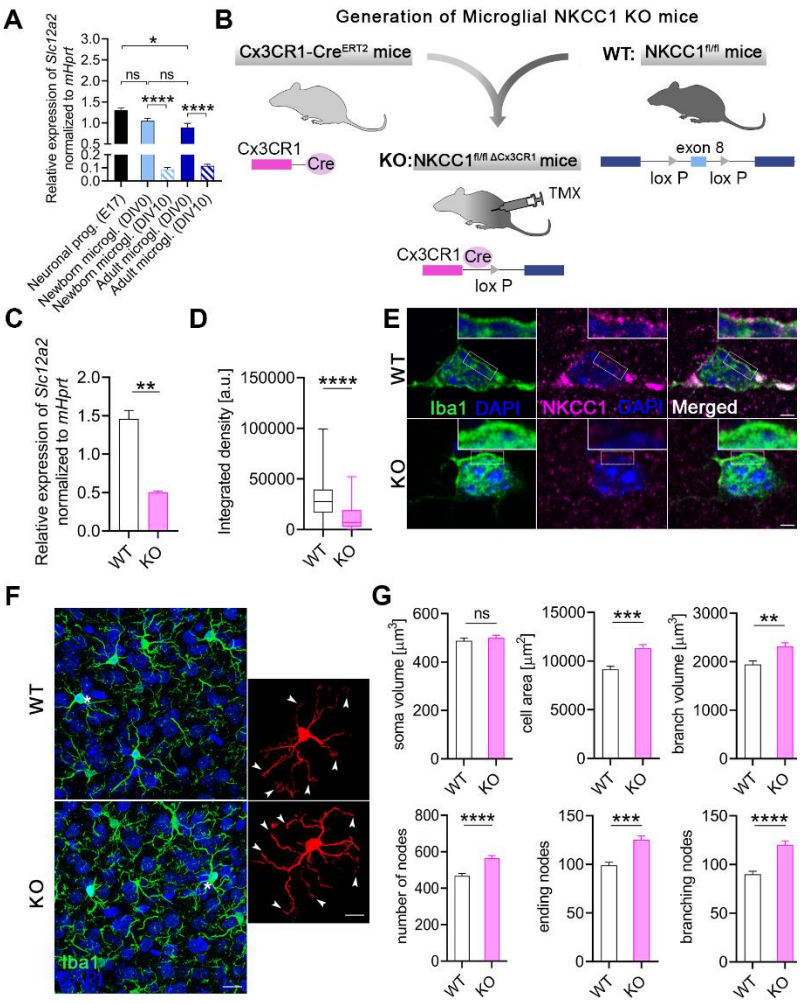

183 **Figure 2. Deletion of microglial NKCC1 markedly impacts on baseline cell morphology and alters**
184 **transformation to reactive microglia. A:** NKCC1 mRNA expression levels in newborn and adult
185 microglia isolated from C57BL/6J mice compared to neural progenitors derived from E17 embryonic
186 hippocampi. Note, that NKCC1 mRNA levels decrease dramatically during *in vitro* maintenance (DIV10).
187 **B:** We generated a novel microglia-specific conditional NKCC1 KO transgenic mouse line by crossing
188 NKCC1$^{fl/fl}$ (exon 8 of the *Slc12a2* gene was flanked with lox P sites) and Cx3CR1-Cre^{ERT2} mice. **C:** NKCC1
189 mRNA levels in isolated NKCC1 KO microglia was markedly reduced in comparison to wild-type cells.
190 **D-E:** NKCC1 protein expression in a large number of randomly sampled NKCC1 KO microglia cells is
191 markedly reduced compared to WT cells. Inserts show plasma membrane localization of NKCC1. **F-G:**
192 Automated morphological analysis and maximum intensity projections of confocal images. Inserts
193 show cells marked with white asterisks in 3D. Arrowheads indicate altered branch structure of NKCC1
194 KO microglia. Automated morphological analysis shows that features of NKCC1 deficient microglia
195 significantly differ from WT microglia. **A:** One-way ANOVA, followed by Holm-Sidak's post hoc test.
196 N=3/group. **: p<0.01; n.s.: not significant **C:** Mann-Whitney test, N=3/group. **: p <0.01 **D:** Mann-
197 Whitney test, N (WT)=142 cells from 2 mice, N (KO)=83 cells from 1 mouse. ****: p<0.0001 **E:** Scale: 2
198 µm **F-G:** Scale: 10 µm; Mann-Whitney test, N (WT)=78 cells from 3 mice, N (KO)=136 cells from 5 mice.
199 **: p <0.01, ***: p <0.001, ****: p <0.0001 Abbreviations: DIV: days in vitro; n.s.: not significant; TMX:
200 tamoxifen
201

202

203 **Microglial process motility is altered by central NKCC1 inhibition**

204 To assess whether NKCC1 is involved in the regulation of dynamic microglial process surveillance and
205 injury-induced microglial responses, we performed *in vivo* two-photon imaging in microglia reporter
206 Cx3CR1$^{+/GFP}$ mice in combination with bumetanide treatment (Figure 3). We tracked pre-lesion
207 (baseline) process motility followed by focal laser-induced lesioning, which was repeated after
208 bumetanide administration into the *cisterna magna* in a different (undisturbed) part of the cerebral
209 cortex in the same animals (Figure 3A-B). Bumetanide caused a small, but significant (7%) increase in
210 the mean velocity of microglial processes (Figure 3C). In contrast, however, lesion-induced recruitment
211 of microglial processes showed a marked, 26,6% reduction after bumetanide treatment (N=6) (Figure
212 3D-E and see **Supplementary Video 1**). These experiments indicate that beyond shaping cell
213 morphology, microglial NKCC1 also regulates dynamic microglial actions both under physiological and
214 pathological conditions.

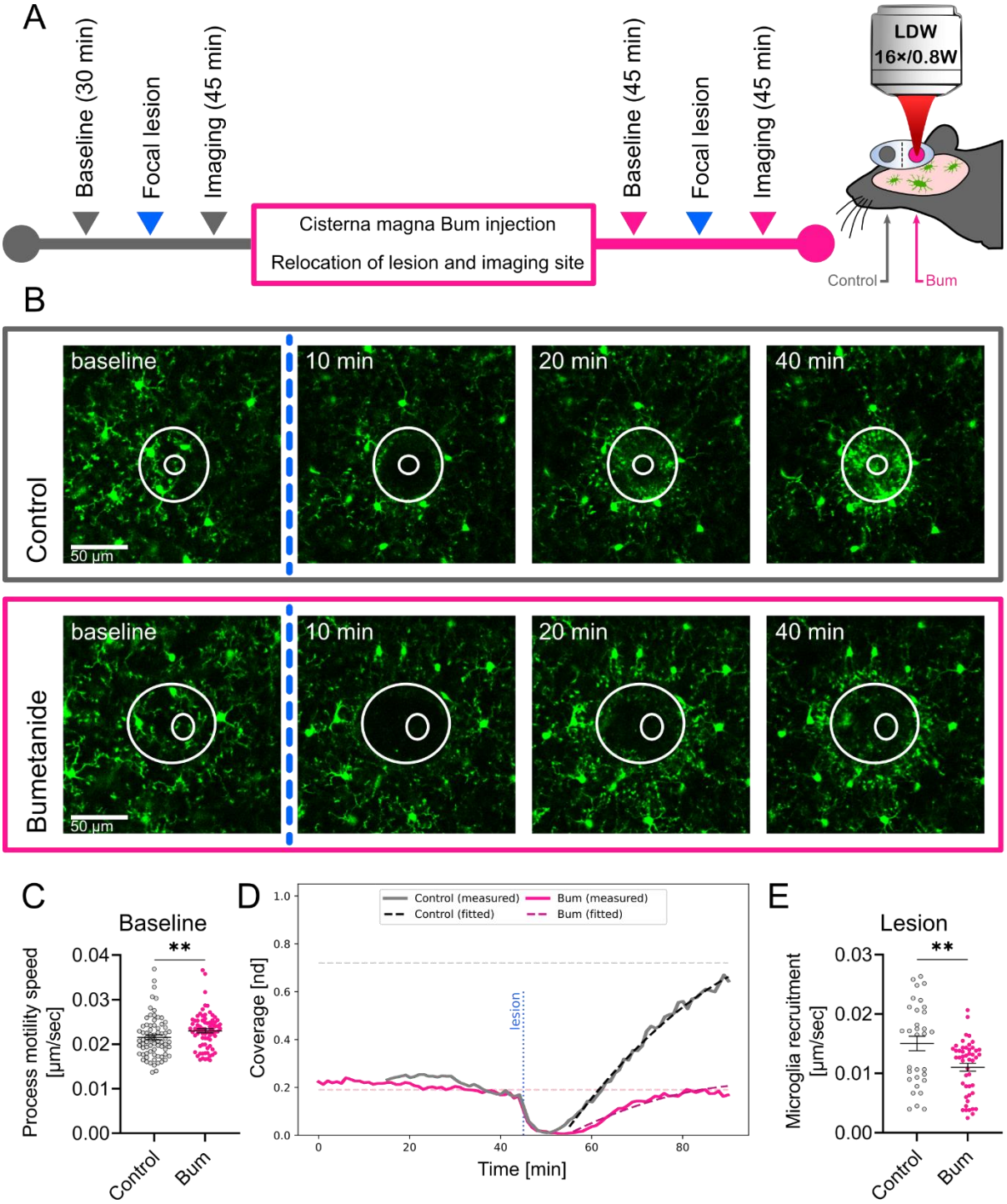

Figure 3. Microglial process dynamics and injury-induced process recruitment are altered by bumetanide A: Outline of the 2-photon imaging experiment performed in Cx3CR1$^{+/GFP}$ (microglia reporter) mice. Imaging was performed to assess baseline microglial process motility and response to laser-induced injury followed by bumetanide administration into the cisterna magna and identical measurements at a different, undisturbed cortical region. **B:** Representative images of microglial responses at selected time points, taken from Supplementary Video 1. The lesion site is marked with circles, but the inner zone of the lesion was excluded from analysis (see Materials and Methods). **C:** Mean base-state velocity distribution of processes from manual image tracking. Data show a 7% higher mean velocity of cell processes after Bum administration. **D:** Evaluation of microglial process coverage

over time in the lesion-centered circular area generated by a custom image analysis pipeline. Solid lines show the proportion of the area covered by microglial GFP signal. Dashed lines show the calculated values of coverage from the best-fitting curves. Horizontal lines are the predicted maximal coverage values for the lesion site, vertical line is the time point of the lesioning. **E:** Calculated post-lesion velocities of microglial process recruitment using automated image analysis followed by model fitting. Data show a significant decrease (26,6%) in mean frontline velocity of cells with Bum administration. **C:** Mann-Whitney test, $N_{Control}$=73, N_{Bum}=76 processes from 5 mice, **: p <0.01 **E:** Mann-Whitney test, $N_{Control}$=32, N_{Bum}=48 fitted values from 4 and 6 mice, respectively, **: p <0.01; Bum: bumetanide

The absence of microglial NKCC1 induces NLRP3 and potentiates inflammatory cytokine production in the cerebral cortex

To assess the effect of NKCC1 deletion on microglial inflammatory states and responses, we first examined the expression of IL-1β and NLRP3. Assembly of the NLRP3 inflammasome is known to be a key step for processing of pro-IL-1β by caspase-1, and the release of mature IL-1β from microglia or macrophages [50,51]. qPCR data revealed elevated expression of both IL-1β and NLRP3 in NKCC1 KO microglia even in the absence of inflammatory stimulus (Figure 4A). Next, we examined the impact of NKCC1 deficiency on morphological characteristics of microglia after activation by endotoxin that primes microglial inflammatory responses and leads to morphological transformation [52]. Unbiased, automated morphological analysis showed that both WT and NKCC1 KO microglia respond to intracortical LPS administration with dramatic morphological conversion (Figure 4C). However, NKCC1-deficient microglia were significantly smaller than their wild type counterparts, displaying a 10% smaller cell surface, 12.5% smaller cell volume and 13.7% smaller branch volume (Figure 4D). According to these data, microglial NKCC1 is likely to be involved in shaping cell morphology and regulation of cell volume after inflammatory challenges.

To test the impact of microglial NKCC1 deletion on the production of central inflammatory mediators, we examined LPS-induced cytokines and chemokines in microglial NKCC1 KO and WT mice twenty-four hours after intracortical LPS injections in brain homogenates (Figure 4E). Importantly, deletion of

255 microglial NKCC1 markedly potentiated LPS-induced levels of G-CSF (3.53-fold), KC (2.12-fold), IL-1α
256 (3.98-fold), IL-1β (3.96-fold), IL-6 (4.35-fold) and TNF-α (3-fold) in the cerebral cortex compared to
257 controls (Figure 4E). In contrast, intracortical LPS treatment did not alter cytokine levels or T cell, B cell,
258 monocyte or granulocyte numbers in the spleen or liver (Supplementary Figure 3A-C). Similarly to that
259 seen after intracortical pharmacological inhibition of NKCC1 by bumetanide, neither the number of
260 $CD11b^{+}$ $CD45^{int}$ microglial cells nor blood-borne $CD11b^{+}$ $CD45^{high}$ leukocytes, $CD11b^{+}$ $Ly6C^{high}$ monocytes
261 or $CD11b^{+}$ $Ly6G^{high}$ granulocytes were altered as a result of microglial NKCC1 deficiency (Figure 4F). We
262 also tested whether increased baseline IL-1β and NLRP3 mRNA levels seen in NKCC1 KO microglia
263 (Figure 4A) were maintained in these cells 24 hours after intracisternal LPS administration. We found
264 that significantly increased NLRP3 mRNA levels (by 100%) were still present in NKCC1 KO microglia
265 isolated from the brain by using magnetic separation, while a strong trend (p=0.057) to increased IL-
266 1β mRNA by 50% was also observed (Figure 4G). These findings corroborated our previous results on
267 cortical NKCC1 blockade by bumetanide, confirming that the inhibition of microglial NKCC1 markedly
268 potentiates central cytokine production upon inflammatory challenges, with a likely role for the NLRP3
269 inflammasome in the excessive production of IL-1β.

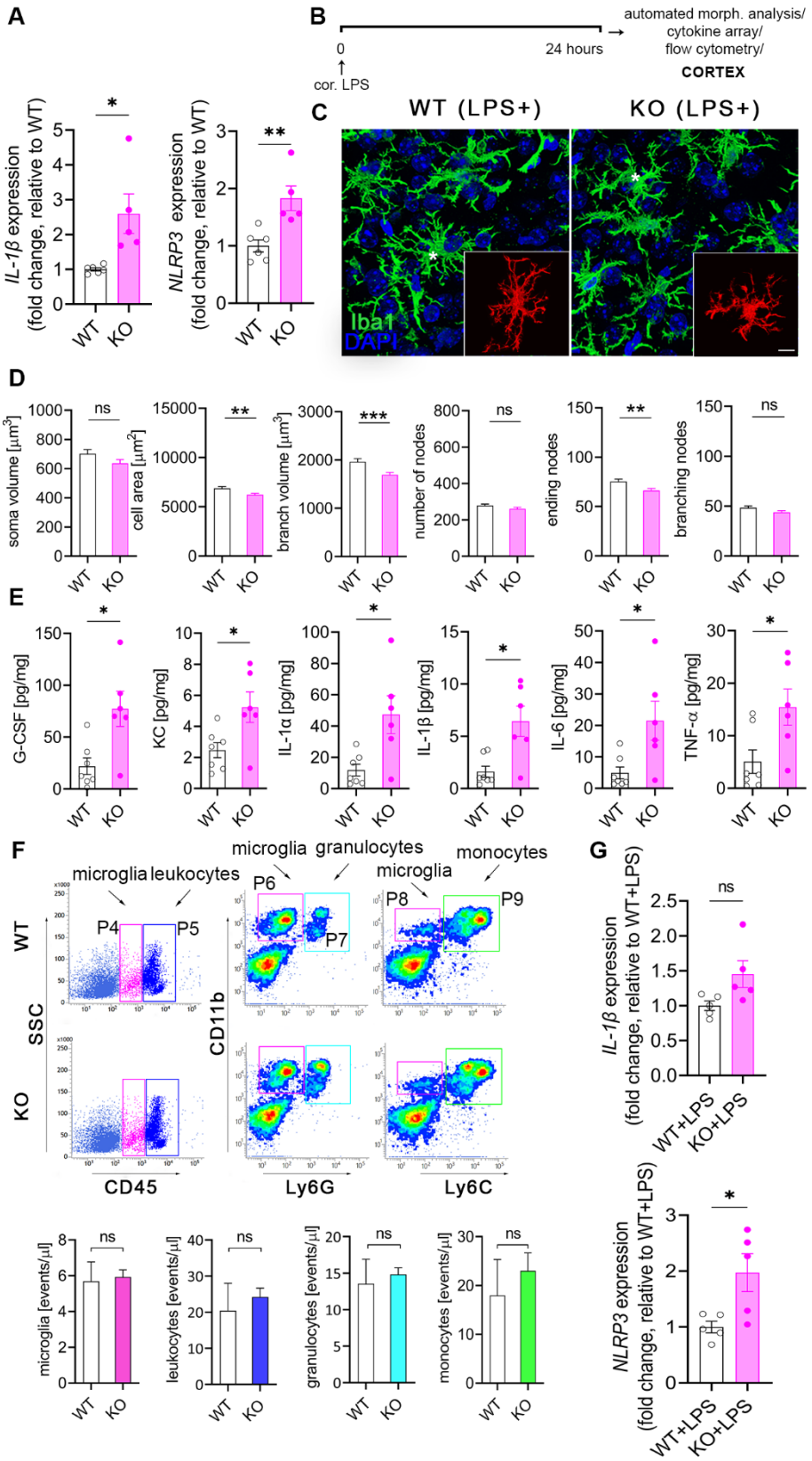

Figure 4. The absence of microglial NKCC1 boosts inflammatory cytokine production in the cerebral cortex in response to an inflammatory stimulus. A: Baseline NLRP3 and IL-1β mRNA expression is increased in isolated NKCC1 KO microglia compared to WT cells. **B:** Experimental outline of automated morphological analysis**,** cytokine array and flow cytometry. **C-D**: Automated morphological analysis

275 show that activated NKCC1 deficient microglia are slightly smaller than their wild-type counterparts.
276 **E**: LPS-induced cytokine levels are significantly higher in the cortices of microglial NKCC1 KO mice than
277 in WT. **F:** Flow cytometric dot plots show that microglial NKCC1 deficiency does not alter the number
278 of $CD11b^+$, $CD45^{int}$ microglia (P4 gate) or numbers of infiltrating $CD11b^+$, $CD45^{high}$ leukocytes (P5 gate),
279 $CD11b^+$, $Ly6C^{high}$ monocytes (P9 gate) and $CD11b^+$, $Ly6G^{high}$ granulocytes (P7 gate) in response to
280 intracortical LPS administration**.** See corresponding data on peripheral cytokine levels and immune cell
281 populations in Supplementary Figure 3**. G:** Increased NLRP3 and IL-1β mRNA levels are sustained in
282 NKCC1 KO and WT microglia 24 hours after intracisternal LPS administration**. A:** Unpaired t-test;
283 **p*<0.05, ***p*<0.01; N (WT)=6, N (KO)=5 **D:** Mann-Whitney test, N (WT)=171 cells from 6 mice, N (KO)=
284 85 cells from 4 mice, ***p*<0.01, ****p*<0.001 **E:** Mann-Whitney test, *: *p* <0.05; N (WT)=7, N (KO)=6 **F:**
285 unpaired t-test, N (WT)=4, N (KO)=4 **G:** Unpaired t-test; **p*<0.05; N (WT)=5, N (KO)=5; n. s.: not
286 significant.
287

288

289 **Deletion of NKCC1 from microglia results in altered membrane currents and decreased intracellular**
290 **Cl^- concentration**

291 To test whether NKCC1 deletion changes ionic gradients across the microglial plasma membrane and
292 alters intracellular ion concentrations, perforated patch-clamp recordings were performed on
293 microglial cells in acute hippocampal slice preparations from WT and NKCC1 KO animals (Figure 5A).
294 This method allows the measurement of membrane currents while intracellular Cl^- concentration
295 remains unchanged. To measure membrane currents, recordings were carried out in voltage-clamp
296 mode at -40 mV holding potential, while a pulse train of voltage steps (-100 mV to 100 mV with 20 mV
297 increments and 100 ms duration) were delivered to construct I-V plots for individual microglial cells.
298 (Figure 5B). I-V curves were obtained both in normotonic and in hypotonic ACSF solution (50% dilution,
299 recorded after 5 min of perfusion). As previously described, an osmotic change due to a hypotonic
300 medium causes microglial cells to stretch, activating volume-regulated anion channels (VRACs) and
301 inducing an outwardly-rectifying current that is mainly driven by Cl^- ions [53–55]. Our measurements
302 showed that both in normotonic and in hypotonic conditions, membrane currents evoked by voltage
303 steps are markedly reduced in microglia with deletion of NKCC1, compared to ones in WT (Figure 5C;
304 WT: N=8, KO: N=8 cells). We also found that resting membrane potentials of microglia in the
305 normotonic condition are significantly more hyperpolarized in the NKCC1 KO compared to WT (Figure

306 5D; WT: N=13, KO: N=12 cells). Furthermore, reversal potential of swelling-induced current (calculated
307 by subtracting the normotonic I-V curve from the hypotonic one) tend to be significantly lower in KO
308 than in WT (Figure 5E). Estimations of intracellular Cl^- ion concentrations based on the swelling-induced
309 current (calculated using the Nernst equation and the reversal potential values of the currents) also
310 suggest that Cl^- ion concentration in microglia lacking NKCC1 is lower than in WT. (Figure 5F).

311
312 To investigate the potential compensatory mechanisms that may arise in response to NKCC1 deletion
313 in microglial cells, we evaluated the expression of some relevant genes that are reportedly expressed
314 by microglia and are known to regulate ion concentrations, membrane potential or response to
315 osmotic stress (Supplementary Figure 4.) *Slc9a1, Slc8a1, Slc12a6, Clic1, Clcn3, Kcnk13, Kcnk6, Kcnj2,*
316 *Kcna3, and Sgk1* mRNAs did not show altered expression between WT and NKCC1 KO microglia, but
317 we found a more than two-fold increase in Lrrc8d, the D subunit of volume regulated anion channel
318 (VRAC) in response to NKCC1 deletion (Supplementary Figure 4A). Importantly, Lrrc8d (VRAC) is
319 involved in increasing the permeability for a broad range of uncharged organic osmolytes [56].
320 Interestingly, intracisternal LPS treatment resulted in a marked reduction of NKCC1 and P2Y12R mRNA
321 levels (Figure 1E), in line with the downregulation of *Slc9a1*, *Slc8a1*, *Lrrc8d*, *Clic1*, *Clcn3*, *Kcnk13*, *Kcnk6*,
322 *Kcnj2*, *Sgk1* genes (Supplementary Figure 4B) of which *Slc9a1, Clic1, Kcna3, Kcnj2, Kcnk13* genes are
323 known to play a role in maintaining ramified morphology and resting state under physiological
324 conditions [35,39,57,58].

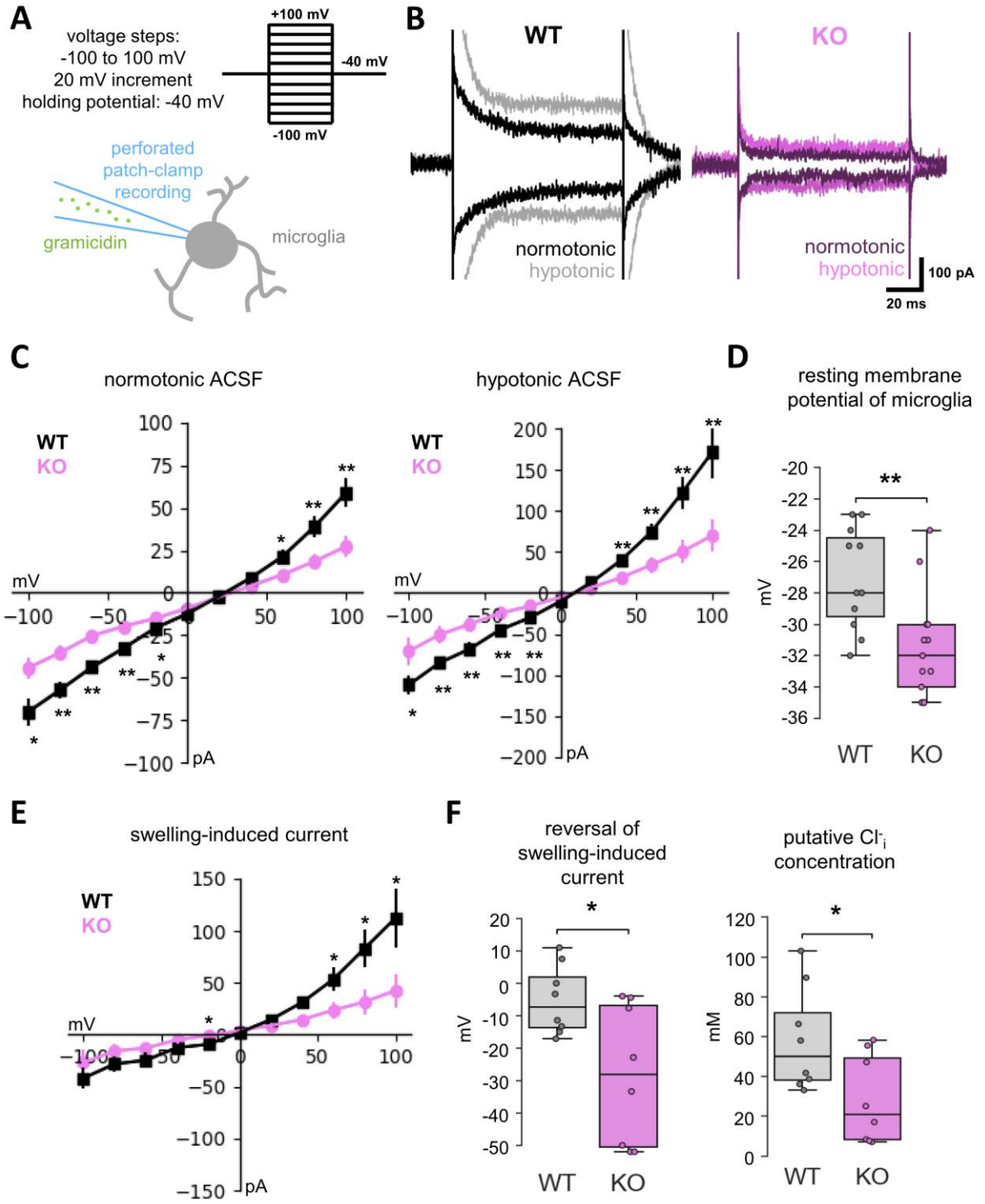

Figure 5. Deletion of NKCC1 from microglia results in altered membrane currents and decreased intracellular Cl- concentration. A: Schematic representation of experiment. Perforated patch-clamp recordings were performed on microglial cells in acute hippocampal slice preparations. Current responses to a train of voltage steps from -100 to 100 mV with 20 mV increments and a duration of 100 ms were measured in voltage-clamp mode (holding potential: -40 mV) both in normotonic, and after 5 minute perfusion with hypotonic ACSF (50% dilution). **B:** Example traces of recordings from WT (black: normotonic, grey: hypotonic ACSF) and NKCC1 KO (purple: normotonic, violet: hypotonic ACSF) animal. Traces show responses for -100 and +100 mV stimulations in both conditions. **C:** Average I-V

334 curve responses from WT (black squares with SEM) and NKCC1 KO cells (violet circles with SEM) in
335 normotonic (left) and after 5 minute perfusion of hypotonic ACSF (right) **D:** Resting membrane
336 potential in normotonic condition of WT vs. NKCC1 KO microglial cells. **E:** I-V curves calculated by the
337 subtraction of measured values in normotonic conditions from ones in hypotonic medium, resulting in
338 I-V curves representing the currents evoked by cell-swelling due to osmotic change. **F:** Reversal
339 potentials of the swelling-induced currents measured from WT (grey) or NKCC1 KO (violet) animals
340 (left), with corresponding intracellular Cl^- concentrations (right) calculated via the Nernst equation. All
341 parametric data are expressed as mean±SEM. **C:** Unpaired t-test; N(WT)=8 cells from 7 animal, N(KO)=8
342 cell from 6 animal; *: p<0.05, **: p<0.01 **D:** Unpaired t-test; N(WT)=13 microglial cells from 12 mice,
343 N(KO)=12 microglial cells from 11 mice; **: *p*<0.01 **E:** Unpaired t-test; *: *p*<0.05 **F:** Unpaired t-test;
344 N(WT)=8 cell, N (KO)=8 cell; *: p<0.05.

345

346

347 **Deletion of microglial NKCC1 increases infarct volume, brain edema and worsens neurological**
348 **outcome after MCAo**

349 Because Na^+-coupled Cl^- importers and their upstream regulatory serine-threonine kinases (WNK-
350 SPAK-OSR1) are involved in maintaining intracellular ionic homeostasis as well as regulation of cell
351 volume [2,49], inhibiting these co-transporters is a subject of interest in ischemic stroke therapy and
352 in other forms of acute brain injury (brain trauma, SAH) where cerebral edema is a major contributor
353 to poor clinical outcome [2,49]. Thus, we investigated whether microglial NKCC1 deficiency influences
354 the severity of brain injury after experimental stroke in microglial NKCC1 KO mice subjected to
355 transient, 45 min long middle cerebral artery occlusion (MCAo). Twenty-four hours after reperfusion,
356 elimination of microglial NKCC1 was not associated with obvious alterations in astroglial GFAP levels
357 or AQP4 levels in perivascular astrocyte endfeet (Supplementary Figure 5). However, we observed a
358 significant increase in brain edema, which was accompanied by a 47% increase in lesion volume (Figure
359 6A-B; *p*=0.0262) and poor neurological outcome in NKCC1 KO mice (Figure 6B; Bederson's score: WT:
360 1.17±0.17, KO: 2.0±0.24; Composit neurological score: WT: 14.9±1.65, KO: 21.9±2.12). Furthermore,
361 experimental stroke induced a 4-fold upregulation of IL-1α and 4.8-fold increase in IL-1β expressing
362 NKCC1 KO microglia cells compared to WT animals, while the overall microglia density and the number
363 of activated microglia were not different at 24 hours reperfusion (Figure 6D-E). We also assessed
364 whether increases in IL-1 production take place early after brain injury before the majority of the

infarct is formed. Cytometric bead array did not reveal altered cytokine production in cortical homogenates shortly (8 hours) after MCAo (Figure 6C). Taken together, these results indicate that microglial NKCC1 deficiency results in augmented brain inflammation, brain edema and increased brain injury after experimental stroke.

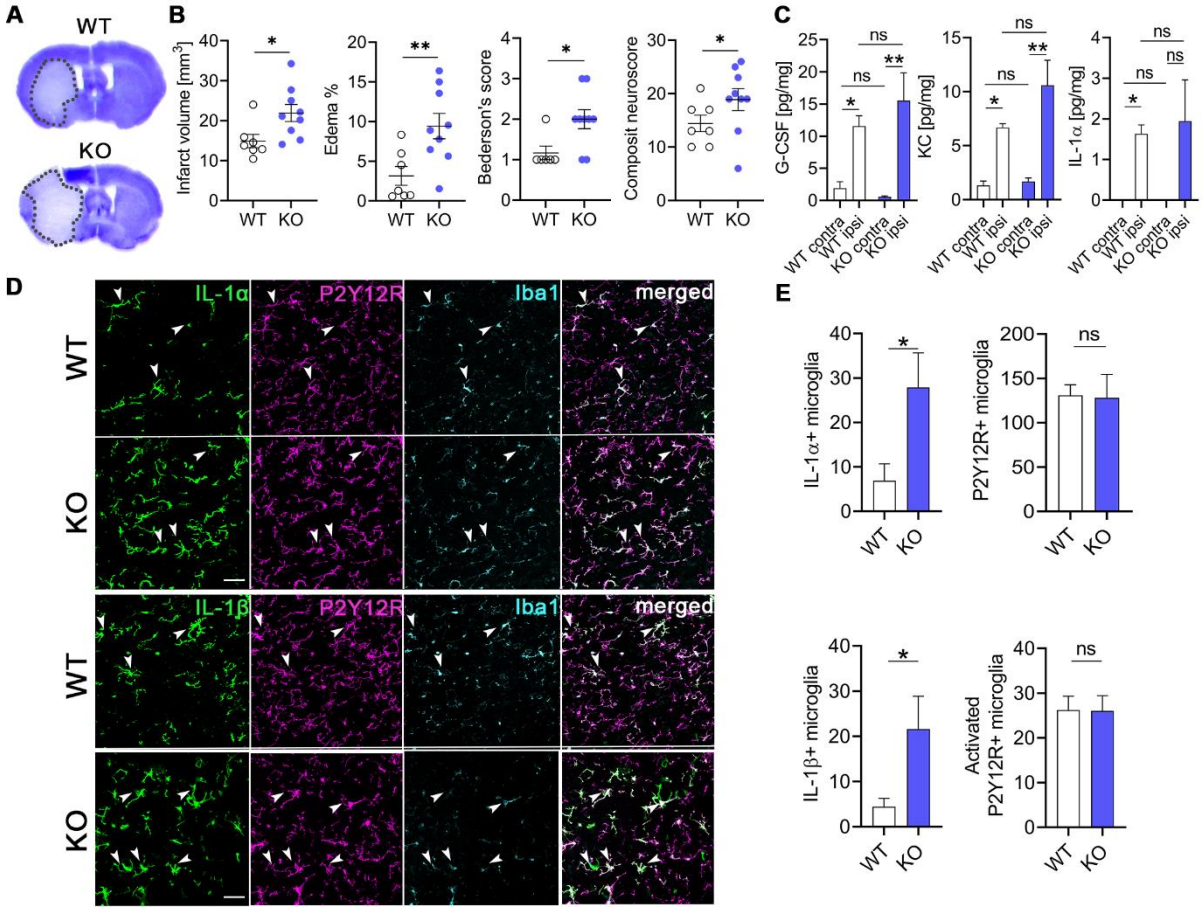

Figure 6. Deletion of microglial NKCC1 increases infarct volume, brain edema and worsens neurological outcome after MCAo. A-B: Microglial NKCC1-deficient mice (KO) show larger infarct volume as assessed on cresyl violet-stained brain sections and more severe neurological outcome compared to wild type mice. **C:** Cytokine levels in the cortex do not differ 8 hours after MCAo in KO mice compared to WT. **D-E:** Microglial NKCC1 deletion results in higher levels of IL-1α and IL-1β 24 hours after MCAo. **B:** Unpaired t-test, N (WT)=7, N (KO)=9; *: $p<0.05$, **: $p<0.01$ **C:** Kruskall-Wallis test followed by Dunn's multiple comparison test; N=6/group. *: $p<0.05$, **: $p<0.01$ **D:** Scale: 50 µm **E:** Mann-Whitney test, *: $p<0.05$; N (WT)=7, N (KO)=9. n.s.: not significant

379 ## Discussion

380 To our knowledge, we show for the first time that NKCC1 is functionally active in microglia in the adult
381 mouse brain and that microglial NKCC1 is involved in shaping both baseline and reactive microglia
382 morphology and responses. We present evidence that NKCC1 regulates microglial membrane
383 potential, chloride levels and adaptation to osmotic stress in a cell-autonomous manner, while the lack
384 of NKCC1 results in primed microglial inflammatory states as evidenced by elevated NLRP3 and IL-1β
385 levels. In line with this, while systemic NKCC1 blockade attenuates LPS-induced inflammation in the
386 brain, central pharmacological inhibition or genetic deletion of microglial NKCC1 potentiates
387 inflammatory cytokine production. Microglial NKCC1 deletion also increases brain injury,
388 inflammation, cerebral edema, and leads to worse neurological outcome after acute brain injury
389 induced by experimental stroke. Thus, microglial NKCC1 emerges as an important regulator of central
390 inflammatory responses.

391 As pointed out in the Introduction, there is little direct information on whether systemically-applied
392 bumetanide might exert therapeutic effects by directly blocking NKCC1 in the brain and, particularly in
393 central neurons. To unravel the effects of pharmacological inhibition of NKCC1 in the periphery and
394 the brain, we investigated the systemic vs. central effects of bumetanide in response to bacterial
395 endotoxin (LPS) administration, which is widely used to trigger inflammatory cytokine responses
396 [41,52]. Intraperitoneally injected bumetanide reduced intracortical LPS-induced proinflammatory
397 cytokine/chemokine responses in the brain, similarly to that found in the case of LPS-induced lung
398 injury attributed to NKCC1-mediated macrophage activation [59]. These findings are also consistent
399 with the suggested beneficial therapeutic effects of systemic NKCC1 blockade in CNS pathologies,
400 which are associated with inflammation [1,7,8,10–12,60].

401 Importantly, intracortical administration of bumetanide had exactly the opposite effect on intracortical
402 LPS-induced cytokine production to that seen after systemic bumetanide treatment, resulting in
403 elevated cytokine levels in the cortex. These markedly different outcomes clearly demonstrate the

404 difficulty to interpret pharmacological interventions in the absence of data on the precise cellular
405 targets of NKCC1 actions in the brain and highlight the need for cell-specific NKCC1 targeting studies.

406 Because microglia are key source of inflammatory cytokine in the brain, we tested whether microglial
407 activity could be directly related to NKCC1 function. Indeed, we observed comparable *Slc12a2*
408 expression in microglia, isolated from either newborn or adult mouse brains, to that seen in neural
409 progenitors. We also revealed NKCC1 protein in cortical microglial cells, which is in line with recent
410 observations showing microglial NKCC1 expression in the superficial spinal dorsal horn in rats [61], as
411 also supported by single-cell transcriptomic studies [21,40]. Further on, we demonstrated that NKCC1
412 levels are markedly downregulated in microglia in response to LPS, alongside with decreased P2Y12R
413 levels (a purinergic receptor regulating microglial cell-cell interactions in response to injury [21,44,62–
414 64]), suggesting that impaired microglial NKCC1 function alters microglial responses to injury or
415 inflammatory stimuli.

416 To investigate the cell-autonomous effects of NKCC1 in microglia, we generated a new, microglial
417 NKCC1 KO transgenic mouse line. We found that the absence of NKCC1 resulted in a more branching
418 microglial morphology in resting state and a more amoeboid shape under inflammatory conditions.
419 These results paralleled enhanced baseline process motility in the intact brain, *in vivo,* and significantly
420 reduced process recruitment to the site of the acute lesion, when microglial NKCC1 was blocked by
421 intracisternal bumetanide during two-photon imaging. Associations of NKCC1 with actin cytoskeleton
422 dynamics [65,66] are well-documented, which take place via controlling F-actin organization through
423 Cofilin-1 and RhoGTPase activity [65]. Thus, our results suggest that regulation of targeted process
424 outgrowth in microglia is NKCC1-dependent, which is known to depend on microglial P2Y12R, but does
425 not require THIK-1, a potassium channel that regulates baseline microglia shape and process motility
426 [35].

427 Importantly, we also found that the absence of microglial NKCC1 renders microglia to express higher
428 levels of NLRP3 and IL-1β mRNA even without any exposure to inflammatory stimuli. It is well-

429 established that changes in microglial membrane potential and ion currents markedly determine cell
430 volume regulation, process dynamics and inflammatory responses of microglia. For example,
431 depolarization is associated with reduced branching in microglia [35,67], while potassium or chloride
432 efflux are essential for NEK7-NLRP3 interaction during the assembly of the NLRP3 inflammasome
433 [38,50], which is required for the production of mature IL-1β [37,38,50]. The regulation of these
434 processes appears to be highly complex. The TWIK2 two-pore domain K^+ channel (K_{2P}) mediates K^+
435 efflux triggering NLRP3 activation in lung macrophages [37], while THIK-1, has been identified as the
436 main K^+ channel in microglia [35], although RNA profiling [21,40] also revealed high expression of
437 TWIK2 in this cell type. In line with this, blocking THIK-1 function inhibits the release of IL-1β from
438 activated microglia, consistent with potassium efflux being necessary for inflammasome activation
439 [35].

440 To investigate how microglial NKCC1 may contribute to these processes, we first investigated whether
441 deletion of NKCC1 leads to altered expression of ion channels or transporters that have been linked
442 with microglial ion- and volume regulation and with inflammatory cytokine production (see references
443 in Supplementary Figure 4D). We could not observe changes in THIK-1 or TWIK2 mRNA levels by qPCR,
444 but the subunit D of volume regulated anion channel (VRAC) was upregulated in KO animals. Subunit
445 D is involved in the transport of uncharged organic osmolytes by VRAC and it may be important for
446 volume-reduction without a major release of inorganic ions [56] for a cell coping with potentially
447 lowered inorganic ion levels due to NKCC1 loss. Interestingly, LRRC8A-containing anion channels are
448 also known associate with NADPH oxidase 1 (Nox1) and regulate superoxide production and TNF-α
449 signalling in vascular smooth muscle cells [56,68]. Thus, changes in microglial ROS production in the
450 absence of NKCC1 will need to be investigated in future studies.

451 Next, we conducted perforated patch-clamp recordings on microglia in acute hippocampal slice
452 preparations from both WT and KO animals. Importantly, we found lower intracellular Cl^-
453 concentrations in the case of NKCC1 KO with resting membrane potentials significantly more

454 hyperpolarized, while membrane currents evoked by voltage steps were markedly reduced in NKCC1
455 KO microglia under both normotonic and hypotonic conditions. Thus, morphological differences in
456 NKCC1 KO microglia may be a direct consequence of altered trafficking of Na^+, K^+ and Cl^- ions through
457 the microglial membrane, which could lead to a more hyperpolarized membrane potential, more
458 ramified morphology, and interference with cell volume regulation and inflammasome activation.
459 Concerning the latter, we found that in line with increased NLRP3 and IL-1β mRNA levels in NKCC1 KO
460 microglia, LPS stimulation resulted in elevated NLRP3 mRNA levels even after 24h upon LPS treatment,
461 and potentiated the production of IL-1β and other cytokines in the cortex of microglial NKCC1 KO mice
462 compared to control mice. Importantly, deletion of microglial NKCC1 had an identical effect on
463 inflammatory cytokine levels to that seen after NKCC1 inhibition by bumetanide, suggesting that
464 central bumetanide actions involve blockade of microglial NKCC1. In line with this, we could not find
465 significant changes in two key astroglial markers, GFAP and AQP4 after central bumetanide application
466 in response to LPS treatment, arguing against a major role of astroglial NKCC1 in the observed
467 differences on the timescale of the present study. While a role for astroglial NKCC1 in mediating central
468 bumetanide actions has been previously reported [18,19], our present work shows that central
469 bumetanide effects involve a substantial microglial component via NKCC1.

470 Proinflammatory cytokine production, particularly the effects mediated by IL-1, are known to influence
471 acute brain injury induced by brain trauma or stroke [69–71]. We found significantly increased infarct
472 volume (by 47%) in microglial NKCC1 KO mice after experimental stroke comparable to a striking, 60%
473 increase in infarct size caused by highly efficient, selective microglia elimination [32]. Microglia
474 depletion resulted in dysregulated neuronal network activity, an effect that is likely to be mediated via
475 elimination of protective microglia-neuron interactions at somatic purinergic junctions [31]. It remains
476 to be investigated in future studies, whether microglia-neuron interactions are altered in microglial
477 NKCC1 KO mice, which could shape neuronal injury via diverse mechanisms related to changes in
478 neuronal excitability [29,30,32,33]. In line with this, the absence of microglial NKCC1 may have

479 contributed to increased neuronal injury via increased IL-1 production, as suggested by the established
480 pathophysiological role of IL-1-mediated actions in different forms of brain injury [69,72].

481 In our experimental stroke studies, we could not detect increased cytokine production in the absence
482 of microglial NKCC1 early (8h) after MCAo, while both IL-1α and IL-1β expression were markedly
483 upregulated in NKCC1 KO microglia 24 hours after reperfusion. Following stroke, impaired cell volume
484 regulation results in cytotoxic cell swelling and edema formation, which peaks beyond the first 24
485 hours in both patients and experimental animals [73,74]. Cerebral edema was shown to be associated
486 with increased phosphorylation of the SPAK/OSR1 kinases playing a key role in NKCC1 activation in
487 various neural cell types [2,48,49] and a SPAK kinase inhibitor, ZT-1a, attenuated cerebral edema after
488 stroke [75]. In line with this, NKCC1 is involved in homeostatic cell volume regulation [48,49] and
489 bumetanide attenuates edema formation in response to ischaemic or traumatic brain injury [2]. In light
490 of these findings, our data showing impaired volume regulation and exaggerated cytokine production
491 in NKCC1 KO microglia have a potentially high pathophysiological and clinical relevance.

492 In conclusion, we show that microglial NKCC1 plays a previously unrecognized role in shaping microglial
493 phenotype and inflammatory responses. Strikingly, bumetanide-induced enhancement of
494 neuroinflammation was mimicked by conditional deletion of microglial NKCC1, suggesting that
495 microglial NKCC1 is a significant target of NKCC1 blockers, given that brain tissue levels of such drugs
496 are sufficiently high [10,13,14]. Our results implying microglial NKCC1 in inflammation, brain edema
497 formation and responses to injury suggest that microglial NKCC1 actions should be considered when
498 studying the effects of NKCC1 inhibitors in different CNS functions and pathologies. This is further
499 emphasized by the broad clinical interest in pharmacological NKCC1 blockade. The present results also
500 call for a re-evaluation of the pharmacological effects of bumetanide in brain diseases with a significant
501 inflammatory component.

502

503 # Materials and Methods

504 **Experimental animals**

505 Experiments were performed on adult male C57BL/6J (RRID: IMSR JAX:000664), NKCC1$^{fl/fl}$ and NKCC1$^{fl/fl}$
506 $^{\Delta\ Cx3CR1}$ (microglial NKCC1 knockout), mice (all on C57BL/6J background). For experiments using LPS
507 treatment P90-110, and for MCAo experiments P70-90 day old mice were used. NKCC1$^{fl/fl}$ mice were
508 kindly provided by Dr. Christian A. Hübner of University Hospital Jena of Friedrich Schiller University,
509 Jena, Germany. Ubiquitous NKCC1 KO mice (P15-20, NKCC1 full knockout, NKCC1$^{-/-}$), generated by
510 crossing C57BL/6NTac-Gt(ROSA)26Sor$^{tm16(cre)Arte}$ and NKCC1$^{fl/fl}$ mice, were used as immunostaining
511 controls and were not subjected to other experimental procedures. Mice were housed in a 12 hours
512 dark/light cycle environment, under controlled temperature and humidity and *ad libitum* access to
513 food and water. All experimental procedures were in accordance with the guidelines set by the
514 European Communities Council Directive (86/609 EEC) and the Hungarian Act of Animal Care and
515 Experimentation (1998; XXVIII, Sect. 243/1998), approved by the Animal Care and Experimentation
516 Committee of the Institute of Experimental Medicine and the Government Office of Pest Country
517 Department of Food Chain Safety, Veterinary Office, Plant Protection and Soil Conservation Budapest,
518 Hungary under the number PE/EA/1021- 7/2019 and Department of Food Chain Safety and Animal
519 Health Directorate of Csongrád Country, Hungary. All experiments followed ARRIVE and IMPROVE
520 guidelines [76,77]. A code was allocated to each animal using GraphPad's random number generator
521 and was randomly assigned to different treatment groups. During all surgical procedures and
522 functional tests the experimenter was blinded to the treatment.

523

524 **Generation and genotyping of the microglial NKCC1 knockout mouse line**

525 Microglial NKCC1 deletion (NKCC1$^{fl/fl\ \Delta Cx3CR1}$) was achieved by crossing tamoxifen-inducible
526 B6.129P2(C)-CX3CR1tm2.1 (cre/ERT2)Jung/J mice (RRID:IMSR_JAX:020940JAX) [78] with the NKCC1$^{fl/fl}$

527 mouse line [79], in which a region between exon 7 and exon 10 of *Slc12a2* gene was flanked with lox
528 P sites. Microglial NKCC1 deletion was achieved by two intraperitoneally administered tamoxifen
529 injections (100 ul of 20mg/ml in corn oil, #T5648, Sigma-Aldrich) 48 hours apart in 3-4 weeks old male
530 mice, shortly after weaning. In all functional experiments mice were studied more than 3 weeks after
531 the last tamoxifen injection to avoid interference with Cre-dependent recombination in peripheral
532 myeloid cells [78]. In the case of selective microglia isolation by magnetic cell sorting, we used animals
533 exposed to tamoxifen for at least two weeks as Cre activity was shown to increase most dramatically
534 within the first week after initiating treatment [80].

535 In all experiments, conditional mutant mice heterozygous for cre and homozygous for NKCC1 flox ($^{cre/+}$
536 $^{fl/fl}$), referred to as NKCC1 KO throughout the manuscript were used. In all cases, littermate controls -
537 referred to as WT - were used which were negative for cre and homozygous for NKCC1 flox ($^{+/+\ fl/fl}$).
538 Heterozygous, conditional mutant mice were viable, fertile, average in size, and did not display any
539 gross physical or marked behavioral abnormalities. Genotypes for *Slc12a2* encoding NKCC1 were
540 determined from tail biopsy samples by conventional PCR using the following primers: 5'-
541 GCAATTAAGTTTGGAGGTTCCTT, 5'- CCAACAGTATGCAGACTCTC and 5'-CCAACAGTATGCAGACTCTC;
542 product sizes: 200 bps for WT, 260 bps for floxed and 460 bps for KO.

543

544 **Microglia cell preparations and cultures**

545 Microglia cells from either newborn (P0-1, male or female) or adult (P40-55, male) C57BL/6J, NKCC1$^{fl/fl}$
546 (WT) or NKCC1$^{fl/fl\ \Delta\ Cx3CR1}$ (KO) mice were isolated by magnetic separation using anti-CD11b microbeads
547 (Miltenyi Biotec, Germany), with slight modification of the protocol described by Otxoa-de-Amezaga
548 [81]. After transcardial perfusion with ice-cold PBS (phosphate buffered saline), the brain tissues
549 (cortices and hippocampi) were enzymatically dissociated with Neural Tissue Dissociation Kit-P (#130-
550 092-628; Miltenyi Biotec). Myelin was removed by MACS Myelin Removal Beads II (#130-096-733,
551 Miltenyi Biotec), then cells in a single-cell suspension were magnetically labeled with MACS CD11b

552 microbeads (#130-093-634, Miltenyi Biotec) and were separated using MS columns (#130-042-201,
553 Miltenyi Biotec, Germany). Cells selected with CD11b microbeads were plated onto poly-L-lysine
554 precoated 96-well or 386-well plates at $3x10^4$ cell/cm^2 density and were cultured at 37 °C in a 95%
555 air/5% CO_2 incubator in DMEM/Glutamax medium (#31966-021, Gibco) supplemented with 10% FBS
556 (fetal bovine serum, #FB-1090, Biosera), 1% Pen/Strep (10000 U/ml; #15140-122, ThermoFisher
557 Scientific) and 10 nM Macrophage Colony-Stimulating Factor (M-CSF; #PMC2044, ThermoFisher
558 Scientific) for 10 days.

559

560 **Embryonic neural progenitor cell preparations**

561 Embryonic hippocampal cells were prepared from C57BL/6J mice on embryonic day 17. After
562 aseptically removing the hippocampi from the skull, tissue was freed from meninges and incubated in
563 0.05% trypsin-EDTA (#T4549, Sigma-Aldrich) solution with 0.05% Dnase I (#DN25, Sigma-Aldrich) in
564 phosphate-buffered saline (PBS) for 15 min at 37°C.

565

566 **Intracortical and intracisternal injections**

567 P90-110 mice were deeply anesthetized with fentanyl (0.05 mg/kg) and mounted into a stereotaxic
568 frame, then were subjected to either single saline or LPS (lipopolysaccharide from *Escherichia coli*
569 O26:B6; 200 nl of 5 mg/ml, rate=200 nl/10 min; #L8274, Sigma-Aldrich) injections using a glass
570 micropipette [82]. The coordinates for the injection were anterior-posterior -2,5 mm, lateral +1,5 mm,
571 and ventral -0,25 mm from the bregma. Bumetanide, a specific inhibitor of NKCC1 was co-injected with
572 LPS (50 µM; #3108, Tocris). At 24h, mice were transcardially perfused with saline, and approximately
573 0.5x0.5x0.5 cm sized tissue pieces from the center of each injected cortical region were cut off and
574 collected for cytokine array and flow cytometric analysis. For tissue sectioning mice were perfused
575 with saline followed by 4% paraformaldehyde in PBS. For qRT-PCR experiments to assess the effect of
576 NKCC1 deficiency on microglial expression of genes which contribute to ion homeostasis, membrane

577 potential, cell volume regulation or inflammation, LPS (5 µg dissolved in ACSF) was administered into
578 the cisterna magna in 5 µl final volume, using a glass capillary. At 24h, mice were transcardially
579 perfused with saline followed by CD11b+ magnetic cell sorting.

580

581 **Systemic administration of LPS and bumetanide**

582 Male adult NKCC1$^{fl/fl}$ mice were injected intraperitoneally with saline, LPS (2 mg/kg; O26:B6, #L8274,
583 Sigma-Aldrich) or LPS (2 mg/kg) and bumetanide (25 mg/kg; #3108, Tocris). Intraperitoneal
584 bumetanide injections were repeated twice, the first one 15 min prior to LPS injection, the second one
585 1 hour after LPS administration. The double injection aimed to ensure that in the critical time window
586 we have effective concentrations of bumetanide in the circulation. At 24h, saline-perfused spleen and
587 brain samples were collected for cytokine measurements or flow cytometric analysis.

588

589 **Cytokine measurement**

590 The levels of inflammatory cytokines and chemokines were measured in spleen and brain samples.
591 Sample processing and protein determination were performed as described previously [83]. Mice were
592 transcardially perfused with saline prior to the collection of spleen and brain samples (ipsilateral to
593 injections). Tissue samples were homogenized in TritonX-100 and protease inhibitor-containing (1:100,
594 #539131, Calbiochem) Tris-HCl buffer (TBS, pH 7.4) and centrifuged at 17000 g, for 20 min at 4 °C.
595 Protein level was quantified for every sample using BCA Protein Assay Kit (#23225, ThermoFisher
596 Scientific). Then, measured cytokine levels were normalized for total protein concentrations. The
597 concentrations of cytokines and chemokines were determined by BD™ Cytometric Bead Array (CBA)
598 using BD CBA Flex Sets (GCSF: #560152, KC: #558340, IL-1α: #560157, IL-1β: #560232, IL-6: #558301,
599 TNF-α: #558299, BD, Becton, Dickinson and Company) according to the manufacturer's instructions.

600 Samples were acquired using a BD FACSVerse flow cytometer (BD, Becton, Dickinson and Company)
601 and the results were analyzed by FCAP Array software (BD, Becton, Dickinson and Company).

602

603 **Flow cytometric analysis of brain and spleen and liver samples**

604 For flow cytometric analysis, cells were isolated from mouse brains with Collagenase D (0,5 mg/ml,
605 #11088866001, Roche), DNase I (10µg/ml, #DN25, Sigma-Aldrich) dissolved in 10% FBS containing
606 DMEM (#6546, Sigma-Aldrich), then the cell suspension was passed through a 40 µm cell strainer
607 (Corning). After enzymatic dissociation, the cells were resuspended in 40% Percoll solution and
608 overlayed on 70% Percoll (#17-0891-01, GE Healthcare). After a density centrifugation step (at 2100
609 rpm, 30 min), mononuclear cells were collected from the interphase of 40%/70% Percoll. Spleen was
610 mechanically homogenized and red blood cells were removed by centrifugation. Before acquisition,
611 brain, spleen and liver cells were diluted with FACS buffer and were incubated with anti-mouse
612 CD16/32 to block Fc receptor. Brain cells or spleen and liver leukocytes were incubated with cocktails
613 of selected antibodies: T cells - anti-mouse CD8a-PE (1:200, #12-0081-82, eBioscience), anti-mouse
614 CD3-APC clone 17A2 (1:200, #17-0032-80, eBioScience), anti-mouse CD4-FITC (1:200, #11-0043-82,
615 eBioscience), anti-mouse CD45-PerCP/Cy5.5 (1:200, #103131, BioLegend); B cells/granulocytes - anti-
616 mouse CD19-FITC (1:200, #11-0193-81, eBioScience), anti-mouse Ly-6C-PE-Cy7 (1:500, #25-5932-80,
617 eBioScience), anti-mouse Ly-6G-APC (1:500, #127613, BioLegend); monocytes/granulocytes - anti-
618 mouse CD11b-FITC (1:200, #11-0112-81, eBioscience); anti-mouse Ly-6C-PE-Cy7; anti-mouse Ly-6G-
619 APC, CD45-PerCP/Cy5.5. To exclude dead cells, some coctails contained propidium iodide (3 µM;
620 #P1304MP, ThermoFisher). Cells were acquired on a BD FACSVerse flow cytometer and data were
621 analyzed using FACSuite software (BD, Becton, Dickinson and Company). Cell counts were calculated
622 by using 15 µm polystyrene microbeads (#18328-5, Polysciences).

623

624 **RNA isolation and cDNA reverse transcription**

625 For qRT-PCR measurements, CD11b+ magnetic sorted microglia cells or embryonic neural progenitor
626 cells were homogenized in QIAzol Lysis Reagent (#79306, QIAGEN) either immediately after isolation
627 or after 10 days of in vitro culturing. Total RNA was isolated using Direct-zol™ RNA Miniprep Kits
628 (#R2052, Zymo Research) following the manufacturer's protocol. The RNA purity and concentration
629 were assessed by NanoDrop ND-1000 spectrophotometer (Nanodrop Technologies). The isolated RNA
630 was then stored at −80 °C. RNA was subjected to DNase I (#AM2224, Ambion) treatment in the
631 presence of RNase H inhibitor (#AM2682, Ambion). Standardized quantities of RNA were reverse
632 transcribed to cDNA using the SuperScript™ II First-strand Reverse Transcriptase system (#18064014,
633 ThermoFisher Scientific) and random hexamers (#48190011, Invitrogen) supplemented with RNase H
634 inhibitor (#AM2682, Ambion).

635

636 **Real-time quantitative PCR (qRT-PCR)**

637 Real-time quantitative PCR was performed with QuantStudio12K Flex qPCR instrument (Applied
638 Biosystems), using TaqMan Gene Expression Assays and the TaqMan Gene Expression Master Mix
639 (#4369016, ThermoFischer Scientific). All mouse TaqMan Gene Expression Assays used for
640 amplification reactions were obtained from ThermoFischer Scientific: *Slc12a2* (Mm01265951_m1,
641 targeting exon 1-10); (Mm00436546_m1, targeting exon 8-10, used for the validation of microglia
642 specific NKCC1 deletion, see Figure 2C), *Hprt* (Mm03024075_m1), *Slc12a6* (Mm01334052_m1), *Slc8a1*
643 (Mm01232254_m1), *Slc9a1* (Mm00444270_m1), *Clcn3* (Mm01348786_m1), *Clic1* (Mm00446336_m1),
644 *Kcnk6* (Mm01176312_g1), *Kcnj2* (Mm00434616_m1), *Kcna3* (Mm00434599_s1), *Lrrc8d*
645 (Mm01207167_m1), *Sgk1* (Mm00441380_m1), *NLRP3* (Mm00840904_m1), *pro-IL-1β*
646 (Mm00434228_m1). The amplification was performed under the following cycling conditions: 95 °C
647 for 10 min, followed by 40 cycles of 95 °C for 10 sec, and 60 °C for 1 min. The comparative Ct method
648 (ΔΔCt method) was used to analyze the relative expression values for each transcript using Hprt as a
649 reference gene.

650 **In vivo two-photon imaging and assessment of microglial process dynamics**

651 CX3CR1$^{+/GFP}$ microglia reporter mice were anaesthetized using fentanyl. As previously has reported
652 [31], fentanyl did not influence microglial process motility compared to the effects of different
653 anaestethics. Cranial window with 3 mm diameter was opened on the left hemisphere centered 1.5
654 mm lateral and 1 mm posterior to bregma without hurting the dura mater. After removal of the skull
655 bone a 3 mm and 5 mm double glass coverslip construct was fixed with 3M™ Vetbond™ tissue glue on
656 top of the dura mater. Then a custom-made metal headpiece (Femtonics Ltd., Budapest, Hungary) was
657 fixed with dental cement on the surface of the skull. All experiments were performed on a Femto2D-
658 DualScanhead microscope (Femtonics Ltd., Budapest, Hungary) coupled with a Chameleon Discovery
659 laser (Coherent, Santa Clara, USA). Following excitation, the fluorescent signal was collected using a
660 Nikon 18X water immersion objective. Data acquisition was performed by MES software (Femtonics
661 Ltd.). Galvano Z-stacks of 8 images (500x500 pixels, 3 µm step size, range=100-125 µm from pial
662 surface) were made at every minute. Two-photon image sequences were exported from MES and
663 analyzed using FIJI. Microglial baseline process velocity was measured on time-series images acquired
664 with 2P microscopy. Following motion correction, images from the same region of CX3CR1$^{+/GFP}$ mice
665 were analyzed with the Manual Tracking plugin of FIJI. We applied a local maximum centring correction
666 method with a search square of 5 pixels. Pixel size was 0.65 µm/px. Processes were included in the
667 measurement when they were clearly traceable for at least 10 minutes. To compare how fast microglia
668 cells are responding to injuries, cortical lesion was formed using laser beam. Focal lesion was induced
669 with an 1040 nm fix laser.

670 Then, we created an automated image processing pipeline using CellProfiler [84] to determine the
671 proportion of area over time covered by microglia cells on each image. The perimeter of the lesion in
672 all image sets was marked manually, and only cells inside this region was taken into account, ignoring
673 also some of the area in the middle as there were autoflourescent artifacts detected there. To
674 differentiate between cells (high intensity areas) and background (low intensity areas), an adaptive

threshold value was calculated from the per-image median intensities. The coverage was then measured as the proportion of pixels classified as cell and the total number of pixels in the image. Coverage values in the initial (baseline) phase of the experiment kept stable, no remarkable oscillation was recorded in any cases. Based on the observed data, we assumed that coverage reaches a minimum value $\varrho_{\min}$ as a result of the injury, then at time t_s, microglia cells start to flow into the lesion area uniformly from its perimeter with velocity v and saturate at a final coverage ϱ_{max}. From this assumption, we created a simple mathematical model that predicts the coverage values over time inside the lesion area.

$$C(t) = (\varrho_{max} - \varrho_{min})\frac{r_o^2 - \left(r_o - v(t - t_s)\right)^2}{r_o^2 - r_i^2} + \varrho_{min}$$

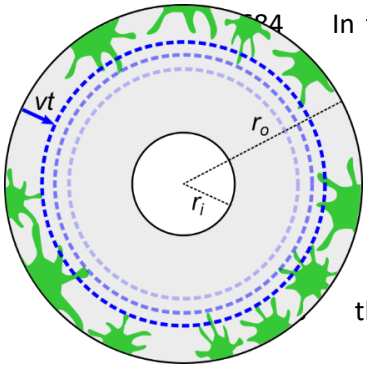

In this equation, r_i and r_o denote the inner and outer radii of the ring-shaped lesion site, respectively. See the inserted drawing for a visual explanation of the model. For each measured coverage dataset, we fitted this model by choosing values for v, q_{max} and t_s that minimize the mean squared difference between the observed and predicted values. To find the best fitting values, a grid search-based optimizer algorithm was used. We found that even this simple model is able to accurately describe the observed behavior of cell flow from the external areas inside the lesion, and it also gives an estimate for the cell's mean velocity which is in good agreement with those from the manual tracking of cell processes.

Middle cerebral artery occlusion (MCAo)

To assess the functional contribution of microglial NKCC1 to ischemic brain injury, mice were subjected to a 45 min long MCAo (Middle Cerebral Artery occlusion) using a silicone-coated filament, as described earlier by Dénes et al. [85]. Surgery was performed under isoflurane (1,5% in a 30% O_2 and 70% N_2O gas mixture) anesthesia and core body temperature was tightly controlled (37 °C ± 0.5 °C)

699 during the whole procedure using a homeothermic heating blanket. Laser Doppler flowmetry was used
700 to validate the occlusion of the MCA. In brief, after a midline incision made on the ventral surface of
701 the neck, the right common carotid artery (CCA) was isolated and a silicone-coated monofilament (210-
702 230 µm tip diameter, Doccol, Sharon, US) was introduced to the left external carotid artery (ECA) and
703 advanced along the internal carotid artery (ICA) to occlude the MCA. Animals were kept in a post-
704 operative chamber at 26-28 °C until the functional assessment having free access to mashed food and
705 water. Neurological outcome was assessed at 24h reperfusion using corner test and the 5-point
706 Bederson's sensory-motor deficit scoring system [86–88]. Briefly, the following scores were given: a 0,
707 no motor deficit; 1, flexion of torso and contralateral forelimb when mouse was lifted by the tail; 2,
708 circling to the contralateral side when mouse is held by the tail on a flat surface, but normal posture
709 at rest; 3, leaning to the contralateral side at rest, 4, no spontaneous motor activity, 5, early death due
710 to stroke. Functional outcome has also been assessed by a complex neurological scoring system to
711 obtain a more comprehensive readout [89]. Results are expressed as composite neurological score.
712 Composite scores range from 0 (healthy mice) to 56 (worst performance) by adding up scores from 13
713 categories as follows: hair (0–2), ears (0–2), eyes (0–4), posture (0–4), spontaneous activity (0–4), and
714 epileptic behavior (0–12), and focal deficits: body symmetry (0–4), gait (0–4), climbing on a surface
715 held at 45° (0–4), circling behavior (0–4), front limb symmetry (0–4), compulsory circling (0–4), and
716 whisker response to a light touch (0–4).

717 Infarct volume and brain edema were calculated after 24h survival on cresyl violet stained coronal
718 brain sections using ImageJ as described previously [90]. In brief, lesion volume was determined at
719 eight neuro-anatomically defined coronal levels (between +2 mm rostral and -4 mm caudal to bregma)
720 by integrating measured areas of damage and correcting for edema size. The pre-determined inclusion
721 criteria for analysis were as follows; decline in Doppler signal of at least 70%, no cerebral hemorrhages
722 and survival to 24 h. Cerebral hemorrhage was identified post-mortem by the presence of excessive
723 bleeding on the external surface of the brain, typically close to the filament location.

724

725 **Immunohistochemistry**

726 ***Perfusion, tissue processing and immunostaining for histology***

727 Mice were anesthetized and transcardially perfused with 0.9% NaCl solution for 1 minute, followed by
728 4% PFA in 0.1 M phosphate buffer (PB) for 40 minutes, followed by 0.1 M PB for 10 minutes to wash
729 the fixative out. Blocks containing the primary somatosensory cortex and dorsal hippocampi were
730 dissected, and coronal sections were prepared on a vibratome (VT1200S, Leica, Germany) at 50 µm
731 thickness for immunofluorescent histological and 100 µm thickness for the automated morphological
732 analysis. Sections were washed in 0.1 M PB, incubated in 10%- and 30%-sucrose containing 0.1 M PB
733 for 3 and 12 hours, respectively. Then the samples were placed into cryovials, snap frozen in liquid
734 nitrogen, and stored at -80 °C for further use. For the free-floating immunohistochemical detection of
735 NKCC1 each vial contained sections from NKCC1$^{fl/fl}$ (WT), NKCC1$^{fl/fl\ \Delta Cx3CR1}$ (KO) and NKCC1$^{-/-}$ mice, which
736 sections were marked by different cuts, enabling that all experimental parameters were completely
737 identical for all samples. The sections were washed in TBS, blocked with a Mouse-on-Mouse blocker
738 solution (MOM blocker, #BMK-2202, Vectorlabs) for 1 hour, washed in TBS 2x5 minutes, washed with
739 MOM-diluent 2x5 minutes. The diluted anti-NKCC1 primary antibodies (NKCC1 Rb: 1:4000, #13884-1-
740 AP, Proteintech, NKCC1 M: 1:2000, diluted in MOM-diluent; DSHB) were pre-incubated for 48 hours
741 with brain slices from NKCC1$^{-/-}$ mice, in order to remove the fraction of immunoglobulins that could
742 potentially cause aspecific-binding. After discarding these slices, the guinea pig anti-Iba1 antibody
743 (#234004, Synaptic Systems) was added to reach a 1:1000 final dilution. This antibody-mixture was
744 applied on the samples for 48 hours at 4 °C during gentle shaking. After intensive washes in TBS,
745 sections were incubated with a mixture of secondary antibodies (donkey-anti mouse Alexa 647,
746 1:1000, #715-605-150; donkey-anti rabbit Alexa 488, 1:1000, #711-546-152; donkey-anti guinea pig
747 Alexa 594, 1:1000, #706-586-148; Jackson ImmunoResearch, diluted in TBS) for 24 hours. After
748 subsequent washes in TBS and 0.1 M PB, DAPI staining was performed and the sections were mounted

749 on glass slides, and covered with Diamond Antifade (#P36961, ThermoFisher) or Aquamount (#18606-
750 5, Polysciences). Immunofluorescence was analyzed using a Nikon Eclipse Ti-E inverted microscope
751 (Nikon Instruments Europe B.V., Amsterdam, The Netherlands), with a CFI Plan Apochromat VC 60X oil
752 immersion objective (numerical aperture: 1.4) and an A1R laser confocal system. We used 405, 488,
753 561 and 647 nm lasers (CVI Melles Griot), and scanning was done in line serial mode. Single image
754 planes were exported from the ND2 files, the outline of microglial cells was drawn using the Iba1-
755 labeling, and the integrated density of the NKCC1 fluorescence signal was measured within these
756 respective ROI-s. This section is related to Figure 2.

757

758 ***Perfusion, processing and immunostaining of ischaemic and LPS-injected tissues***

759 In terminal ketamine-xylazine anesthesia (100 mg/kg-10 mg/kg) mice were transcardially perfused
760 with 0.9% NaCl solution, followed by 4% phosphate buffered PFA. Brains of microglial NKCC1 KO mice
761 subjected to 45 min MCAo were postfixed and cryoprotected overnight (in 4% phosphate buffered
762 PFA-10% sucrose solution), then immersed into a cryoprotective solution (10% sucrose in PBS) at least
763 2h before 25 µm coronal sections were cut using a sledge microtome. Immunofluorescent staining was
764 performed on free-floating coronal brain sections. Brain sections were blocked with 5% normal donkey
765 serum followed by overnight incubation at 4 °C using the following mixture of primary antibodies: goat
766 anti-IL-1β/ILF2 (1:250; #AF-401-NA, R&D Systems), rat anti-CD45 (1:250; #MCA1388, AbD Serotec),
767 rabbit anti-P2Y12R (1:500; #55043AS, AnaSpec). After the incubation with the primaries, sections were
768 washed several times in TBS and were incubated with mixture of corresponding secondary antibodies
769 at room temperature for 2h. The following secondaries were used: donkey-anti goat CF568 (1:1000;
770 #20106, Biotium), donkey-anti rabbit Alexa 647 (1:1000; #711-605-152, Jackson ImmunoResearch),
771 donkey-anti rat Alexa 488 (1:1000; #712-546-153, Jackson ImmunoResearch). Slices were washed in
772 TBS and were mounted to microscope slides using Fluoromount-G (#0100-01, SouthernBiotech).
773 Representative images were captured with a 20X objective (Plan Apo VC, numerical aperture: 0,.75,

774 FOV=645.12um) on a Nikon A1R confocal system. Quantitative analysis was performed on widefield
775 images, captured with a 20X objective (Plan, numerical aperture: 0.4) on a Nikon Eclipse Ti-E inverted
776 microscope (Nikon Instruments Europe B.V., Amsterdam, The Netherlands). IL-1α and IL-1β positive
777 cells in the penumbral region, P2Y12R positive and CD45 positive cells in the whole cortex were
778 counted on 3-3 serial coronal sections for a given brain area. This methodical description is related to
779 Figure 4.

780 The following primaries and secondaries were used for GFAP and AQP4 immunolabeling: chicken anti-
781 GFAP (1:1000, #173006, Synaptic Systems) and guinea pig anti-AQP4 (1:500, #429004, Synaptic
782 Systems), donkey anti-chicken A594 (1:500, #703-586-155, Jackson ImmunoResearch) and donkey
783 anti-guinea pig A647 (1:500, #706-606-148, Jackson ImmunoResearch). For imaging, fluorescent slide
784 scanner (Panoramic MIDI 3D HISTECH) with 20X Plan-Apochromat objective was used. Raw integrated
785 densities were automatically measured on all images in selected ROIs from the striatum, and then their
786 per-animal average was calculated and used for statistical analysis. This methodical description is
787 related to Supplementary Figure 2 and 5.

788

789 **Electrophysiology**

790 ***Slice preparation***

791 In all cases, mice (56-65 days) were decapitated under deep isoflurane anaesthesia. The brain was
792 removed and placed into an ice-cold cutting solution, which had been bubbled with 95% O_2–5% CO_2
793 (carbogen gas) for at least 30 min before use. The cutting solution contained the following (in mM):
794 205 sucrose, 2.5 KCl, 26 $NaHCO_3$, 0.5 $CaCl_2$, 5 $MgCl_2$, 1.25 NaH_2PO_4, 10 glucose, saturated with 95% O_2–
795 5% CO_2. Horizontal hippocampal slices of 250 µm thickness were cut using a Vibratome (Leica
796 VT1000S). Slices were placed into an interface-type incubation chamber which contained standard
797 ACSF at 35°C that gradually cooled down to room temperature. At the beginning of the incubation
798 period, a solution of 25µm/ml Alexa 594 conjugated isolectin B4 (I21413, ThermoFisher) diluted in

799 ACSF was pipetted on top of each slice (15 ml/slice). After this, slice preparations were incubated in
800 darkness for 1 hour before measurement. All measurements took place within 4 hours after slicing.
801 The ACSF solution contained the following (in mM): 126 NaCl, 2.5 KCl, 26 $NaHCO_3$, 2 $CaCl_2$, 2 $MgCl_2$,
802 1.25 NaH_2PO4, 10 glucose, saturated with 95% O_2–5% CO_2.

803 ***Recording conditions***

804 After incubation for at least 1 hour, slices were transferred individually into a submerged-type
805 recording chamber with a superfusion system allowing constantly bubbled (95% O_2–5% CO_2) ACSF to
806 flow at a rate of 3-3.5 ml/min. The ACSF solution in all cases was adjusted to 300-305 mOsm to have a
807 consistent normotonic medium during experiments, and in the hypotonic condition the same solution
808 was diluted to have 50% the osmolarity of normotonic solution. Both normotonic and hypotonic ACSF
809 solutions were constantly saturated with 95% O_2–5% CO_2 during measurements. All measurements
810 were carried out at room temperature. A stock solution of 100 mg/ml gramicidin B (G5002, Sigma-
811 Aldrich) diluted in DMSO was prepared daily, and further diluted to 100 µg/ml concentration in filtered,
812 intracellular solution. Alexa 488 (100 µM) was also added to monitor membrane integrity during
813 measurements. Before each recording, standard patch pipettes were fabricated from borosilicate glass
814 and prefilled with gramicidin free intracellular solution, and then backfilled with the intracellular
815 solution containing gramicidin and Alexa 488. The intracellular solution contained the following (in
816 mM): 120 KCl, 1 $CaCl_2$, 2 $MgCl_2$, 10 HEPES, and 11 EGTA, pH: 7.3, 280-300 mOsm. Standard patch
817 electrodes were used in all of the recordings, pipette resistances were 3-6 MΩ when filled with
818 intracellular solution. Visualization of slices and selection of cells (guided by isolectin B signal) were
819 carried out under an upright microscope (BX61WI; Olympus, Tokyo, Japan equipped with infrared-
820 differential interference contrast optics and a UV lamp). Only cells below 15-20 µm measured from
821 slice surface were targeted. During recordings, Alexa 488 signal was constantly monitored, to make
822 sure that the membrane of cells did not suffer a rupture. Those cells who developed Alexa 488 signal
823 in their cell body, were automatically discarded. All cells were recorded in voltage-clamp mode at -40

824 mV holding potential. Series resistance was constantly monitored and perforation was considered to
825 be formed when values decreased to the 35-50 MΩ range (this regularly happened after 25-30 minutes
826 after Gigaseal formation), and showed stability in series resistance and current response values
827 between a 15% margin during the whole recording. Cells exceeding their initial value of series
828 resistance and current responses measured at the beginning of both normotonic and hypotonic
829 conditions beyond 15% in either directions during recordings were discarded. Input resistance of cells
830 were 4.75 GΩ ± 1.56 SEM in WT and 3.94 GΩ ± 0.97 SEM in NKCC1 KO animals. There was no significant
831 difference in input resistance values of measured cells between WT and NKCC1 KO animals
832 (independent t-test, p=0.33). A pulse train ranging from -100 mV to 100 mV with 20 mV increments
833 were recorded, each stimulus was 100 ms in length, and repeated 3 times. Gaps between pulses were
834 2000 ms in length. Pulse trains were recorded in the normotonic ACSF when stable perforated patch-
835 clamp mode was established, and after 5 minutes of perfusion with hypotonic ACSF (50% dilution).
836 Recordings were performed with a Multiclamp 700B amplifier (Molecular Devices). Data were digitized
837 at 10 kHz with a DAQ board (National Instruments, USB-6353) and recorded with a custom software
838 developed in C#.NET and VB.NET in the laboratory. Analysis was done using custom software
839 developed in Delphi and Python environments.

840

841 **Automated morphological analysis of microglial cells**

842 100 µm thick mouse brain coronal sections were immunostained with guinea pig anti-Iba1 (1:500;
843 #234004, Synaptic Systems), Alexa 647 donkey anti-guinea pig (1:500; #706-606-148, Jackson
844 ImmunoResearch) antibodies, and DAPI. Imaging was carried out in 0.1M PB, using a Nikon Eclipse Ti-
845 E inverted microscope (Nikon Instruments Europe B.V., Amsterdam, The Netherlands), with a CFI Plan
846 Apochromat VC 60X water immersion objective (numerical aperture: 1.2) and an A1R laser confocal
847 system. For 3-dimensional morphological analysis of microglial cells, the open-source MATLAB-based
848 Microglia Morphology Quantification Tool was used (available at

849 https://github.com/isdneuroimaging/mmqt). This method uses microglia and cell nuclei labeling to
850 identify microglial cells. Briefly, 59 possible parameters describing microglial morphology are
851 determined through the following automated steps: identification of microglia (nucleus, soma,
852 branches) and background, creation of 3D skeletons, watershed segmentation and segregation of
853 individual cells [47].

854

855 **Quantification and Statistical analysis**

856 All quantitative assessment was performed in a blinded manner. Based on the type and distribution of
857 data populations (examined with Shapiro-Wilk normality tests) we applied appropriate statistical tests:
858 In the case of two independent groups, Student's t-test or Mann-Whitney U-test, for three or more
859 independent groups one-way ANOVA followed by Tukey's *post hoc* comparison or Kruskal-Wallis test
860 with Dunn's multiple comparison test was applied. Data were analyzed using the GraphPad Prism
861 version 8.2 for Windows software (GraphPad Software, San Diego, California USA). In this study, data
862 are expressed as mean±SEM, $p<0.05$ was considered statistically significant.

863

864

865 ## Acknowledgments

866 This work was supported by „Momentum" research grant from the Hungarian Academy of Sciences
867 (LP2016-4/2016 to A.D.) and ERC-CoG 724994 (to A.D.). Additionally, this work was funded by
868 Hungarian National Scientific Research Fund (NKFIH-OTKA Grant No. K131844 to S.B.), the János Bolyai
869 Research Scholarship of the Hungarian Academy of Sciences (to N.L. and C.C.), ÚNKP-20-3-II (to B.P.)
870 and ÚNKP-20-5 (to C.C.) of the New National Excellence Program of the Ministry for Innovation and
871 Technology, Hungary; and German Research Foundation (SPP 1665) and the Federal Ministry of
872 Education and Research (NEURON ACRoBAT) to C.A.H. A.A. holds a Stipendium Hungaricum

Scholarship from the Government of Hungary. We thank László Barna and the Nikon Imaging Center at the Institute of Experimental Medicine for kindly providing microscopy support, and thank Dóra Gali-Györkei for her excellent technical assistance.

Author Contributions

Experimental design and overall concept, A.D. and Zs.K; Methodology, C.A.H.; N.L.; E.S.; P.B.; A.G.; Formal Analysis K.T.; N.L., B.P., S.B.; P.B.; D.K.; Investigation, K.T., N.L., B.P., R.F., E.S., A.A., C.C, Zs.K.; P.B.; Resources, A.D., S.B., C.A.H; Writing – Original Draft, K.T., Zs.K., A.D., Writing – Review & Editing K.T.; Zs.K., K.K., A.D. with all authors; Intellectual contribution, conceptual support K.K., C.A.H; Visualization K.T., E.S., C.C., B.P. D.K.; Supervision A.D. and Zs.K.; Project Administration A.D. and Zs.K.; Funding Acquisition, A.D.

Competing interests

The authors declare no competing interests.

References

1. Kaila K, Price TJ, Payne JA, Puskarjov M, Voipio J. Cation-chloride cotransporters in neuronal development, plasticity and disease. Nat Rev Neurosci. 2014;15: 637–654. doi:10.1038/nrn3819
2. Huang H, Song S, Banerjee S, Jiang T, Zhang J, Kahle KT, et al. The WNK-SPAK/OSR1 Kinases and the Cation-Chloride Cotransporters as Therapeutic Targets for Neurological Diseases. Aging Dis. 2019;10: 626. doi:10.14336/ad.2018.0928
3. Huberfeld G, Wittner L, Clemenceau S, Baulac M, Kaila K, Miles R, et al. Perturbed chloride homeostasis and GABAergic signaling in human temporal lobe epilepsy. J Neurosci. 2007;27: 9866–9873. doi:10.1523/JNEUROSCI.2761-07.2007
4. Kaila K, Ruusuvuori E, Seja P, Voipio J, Puskarjov M. GABA actions and ionic plasticity in epilepsy. Current Opinion in Neurobiology. Elsevier Current Trends; 2014. pp. 34–41. doi:10.1016/j.conb.2013.11.004
5. Shekarabi M, Zhang J, Khanna AR, Ellison DH, Delpire E, Kahle KT. WNK Kinase Signaling in Ion Homeostasis and Human Disease. Cell Metabolism. Cell Press; 2017. pp. 285–299. doi:10.1016/j.cmet.2017.01.007
6. Schulte JT, Wierenga CJ, Bruining H. Chloride transporters and GABA polarity in developmental, neurological and psychiatric conditions. Neuroscience and

905 Biobehavioral Reviews. Elsevier Ltd; 2018. pp. 260–271.
906 doi:10.1016/j.neubiorev.2018.05.001

907 7. Ben-Ari Y. NKCC1 Chloride Importer Antagonists Attenuate Many Neurological and
908 Psychiatric Disorders. Trends in Neurosciences. Elsevier Ltd; 2017. pp. 536–554.
909 doi:10.1016/j.tins.2017.07.001

910 8. Kharod SC, Kang SK, Kadam SD. Off-label use of bumetanide for brain disorders: An
911 overview. Frontiers in Neuroscience. Frontiers Media S.A.; 2019.
912 doi:10.3389/fnins.2019.00310

913 9. Lemonnier E, Degrez C, Phelep M, Tyzio R, Josse F, Grandgeorge M, et al. A
914 randomised controlled trial of bumetanide in the treatment of autism in children.
915 Transl Psychiatry. 2012;2: 202. doi:10.1038/tp.2012.124

916 10. Puskarjov M, Kahle KT, Ruusuvuori E, Kaila K. Pharmacotherapeutic targeting of
917 cation-chloride cotransporters in neonatal seizures. Epilepsia. Blackwell Publishing
918 Inc.; 2014. pp. 806–818. doi:10.1111/epi.12620

919 11. Löscher W, Puskarjov M, Kaila K. Cation-chloride cotransporters NKCC1 and KCC2 as
920 potential targets for novel antiepileptic and antiepileptogenic treatments.
921 Neuropharmacology. Pergamon; 2013. pp. 62–74.
922 doi:10.1016/j.neuropharm.2012.05.045

923 12. Töllner K, Brandt C, Töpfer M, Brunhofer G, Erker T, Gabriel M, et al. A novel prodrug-
924 based strategy to increase effects of bumetanide in epilepsy. Ann Neurol. 2014;75:
925 550–562. doi:10.1002/ana.24124

926 13. Töllner K, Brandt C, Römermann K, Löscher W. The organic anion transport inhibitor
927 probenecid increases brain concentrations of the NKCC1 inhibitor bumetanide. Eur J
928 Pharmacol. 2015;746: 167–173. doi:10.1016/j.ejphar.2014.11.019

929 14. Römermann K, Fedrowitz M, Hampel P, Kaczmarek E, Töllner K, Erker T, et al. Multiple
930 blood-brain barrier transport mechanisms limit bumetanide accumulation, and
931 therapeutic potential, in the mammalian brain. Neuropharmacology. 2017;117: 182–
932 194. doi:10.1016/j.neuropharm.2017.02.006

933 15. Virtanen MA, Uvarov P, Hübner CA, Kaila K. NKCC1, an Elusive Molecular Target in
934 Brain Development: Making Sense of the Existing Data. Cells. 2020;9: 2607.
935 doi:10.3390/cells9122607

936 16. Wang H, Yan Y, Kintner DB, Lytle C, Sun D. GABA-mediated trophic effect on
937 oligodendrocytes requires Na-K-2Cl cotransport activity. J Neurophysiol. 2003;90:
938 1257–1265. doi:10.1152/jn.01174.2002

939 17. Yu Y, Fu P, Yu Z, Xie M, Wang W, Luo X. NKCC1 Inhibition Attenuates Chronic Cerebral
940 Hypoperfusion-Induced White Matter Lesions by Enhancing Progenitor Cells of
941 Oligodendrocyte Proliferation. J Mol Neurosci. 2018;64: 449–458.
942 doi:10.1007/s12031-018-1043-0

943 18. Henneberger C, Bard L, Panatier A, Reynolds JP, Kopach O, Medvedev NI, et al. LTP
944 Induction Boosts Glutamate Spillover by Driving Withdrawal of Perisynaptic Astroglia.
945 Neuron. 2020 [cited 15 Nov 2020]. doi:10.1016/j.neuron.2020.08.030

946 19. Noor ZN, Deitmer JW, Theparambil SM. Cytosolic sodium regulation in mouse cortical

947 astrocytes and its dependence on potassium and bicarbonate. J Cell Physiol.
948 2019;234: 89–99. doi:10.1002/jcp.26824

949 20. Su G, Kintner DB, Flagella M, Shull GE, Sun D. Astrocytes from Na+-K+-Cl-
950 cotransporter-null mice exhibit absence of swelling and decrease in EAA release. Am J
951 Physiol - Cell Physiol. 2002;282. doi:10.1152/ajpcell.00538.2001

952 21. Zhang Y, Chen K, Sloan SA, Bennett ML, Scholze AR, O'Keeffe S, et al. An RNA-
953 sequencing transcriptome and splicing database of glia, neurons, and vascular cells of
954 the cerebral cortex. J Neurosci. 2014;34: 11929–11947. doi:10.1523/JNEUROSCI.1860-
955 14.2014

956 22. Kaila K, Price TJ, Payne JA, Puskarjov M, Voipio J. Cation-chloride cotransporters in
957 neuronal development, plasticity and disease. Nature Reviews Neuroscience. Nature
958 Publishing Group; 2014. pp. 637–654. doi:10.1038/nrn3819

959 23. Huang LQ, Zhu GF, Deng YY, Jiang WQ, Fang M, Chen CB, et al. Hypertonic saline
960 alleviates cerebral edema by inhibiting microglia-derived TNF-α and IL-1β-induced Na-
961 K-Cl Cotransporter up-regulation. J Neuroinflammation. 2014;11. doi:10.1186/1742-
962 2094-11-102

963 24. Pozdeev VI, Lang E, Görg B, Bidmon HJ, Shinde P V., Kircheis G, et al. TNFα induced up-
964 regulation of Na+,K+,2Cl− cotransporter NKCC1 in hepatic ammonia clearance and
965 cerebral ammonia toxicity. Sci Rep. 2017;7. doi:10.1038/s41598-017-07640-8

966 25. Reid AY, Riazi K, Campbell Teskey G, Pittman QJ. Increased excitability and molecular
967 changes in adult rats after a febrile seizure. Epilepsia. 2013;54. doi:10.1111/epi.12061

968 26. Weidenfeld S, Kuebler WM. Cytokine-regulation of Na+-K+-Cl- cotransporter 1 and
969 cystic fibrosis transmembrane conductance regulator-potential role in pulmonary
970 inflammation and edema formation. Frontiers in Immunology. Frontiers Research
971 Foundation; 2017. p. 393. doi:10.3389/fimmu.2017.00393

972 27. Salter MW, Stevens B. Microglia emerge as central players in brain disease. Nat Med
973 2017 239. 2017;23: 1018–1027. doi:10.1038/nm.4397

974 28. Song WM, Colonna M. The identity and function of microglia in neurodegeneration.
975 Nature Immunology. Nature Publishing Group; 2018. pp. 1048–1058.
976 doi:10.1038/s41590-018-0212-1

977 29. Wu W, Li Y, Wei Y, Bosco DB, Xie M, Zhao MG, et al. Microglial depletion aggravates
978 the severity of acute and chronic seizures in mice. Brain Behav Immun. 2020;89: 245–
979 255. doi:10.1016/j.bbi.2020.06.028

980 30. Badimon A, Strasburger HJ, Ayata P, Chen X, Nair A, Ikegami A, et al. Negative
981 feedback control of neuronal activity by microglia. Nature. 2020;586: 417–423.
982 doi:10.1038/s41586-020-2777-8

983 31. Cserép C, Pósfai B, Lénárt N, Fekete R, László ZI, Lele Z, et al. Microglia monitor and
984 protect neuronal function through specialized somatic purinergic junctions. Science
985 (80-). 2020;367: 528–537. doi:10.1126/science.aax6752

986 32. Szalay G, Martinecz B, Lénárt N, Környei Z, Orsolits B, Judák L, et al. Microglia protect
987 against brain injury and their selective elimination dysregulates neuronal network
988 activity after stroke. Nat Commun. 2016;7: 11499. doi:10.1038/ncomms11499

989 33. Eyo UB, Peng J, Swiatkowski P, Mukherjee A, Bispo A, Wu L-J. Neuronal hyperactivity
990 recruits microglial processes via neuronal NMDA receptors and microglial P2Y12
991 receptors after status epilepticus. J Neurosci. 2014;34: 10528–40.
992 doi:10.1523/JNEUROSCI.0416-14.2014

993 34. Ayata C, Lauritzen M. Spreading depression, spreading depolarizations, and the
994 cerebral vasculature. Physiol Rev. 2015;95: 953–993. doi:10.1152/physrev.00027.2014

995 35. Madry C, Kyrargyri V, Arancibia-Cárcamo IL, Jolivet R, Kohsaka S, Bryan RM, et al.
996 Microglial Ramification, Surveillance, and Interleukin-1β Release Are Regulated by the
997 Two-Pore Domain K + Channel THIK-1. Neuron. 2018;97: 299-312.e6.
998 doi:10.1016/j.neuron.2017.12.002

999 36. Nguyen HM, Grössinger EM, Horiuchi M, Davis KW, Jin L-W, Maezawa I, et al.
1000 Differential Kv1.3, KCa3.1, and Kir2.1 expression in "classically" and "alternatively"
1001 activated microglia. Glia. 2017;65: 106–121. doi:10.1002/glia.23078

1002 37. Di A, Xiong S, Ye Z, Malireddi RKS, Kometani S, Zhong M, et al. The TWIK2 Potassium
1003 Efflux Channel in Macrophages Mediates NLRP3 Inflammasome-Induced
1004 Inflammation. Immunity. 2018;49: 56-65.e4. doi:10.1016/j.immuni.2018.04.032

1005 38. He Y, Zeng MY, Yang D, Motro B, Núñez G. NEK7 is an essential mediator of NLRP3
1006 activation downstream of potassium efflux. Nature. 2016;530: 354–357.
1007 doi:10.1038/nature16959

1008 39. Tang T, Lang X, Xu C, Wang X, Gong T, Yang Y, et al. CLICs-dependent chloride efflux is
1009 an essential and proximal upstream event for NLRP3 inflammasome activation. Nat
1010 Commun. 2017;8. doi:10.1038/s41467-017-00227-x

1011 40. Bennett ML, Bennett FC, Liddelow SA, Ajami B, Zamanian JL, Fernhoff NB, et al. New
1012 tools for studying microglia in the mouse and human CNS. Proc Natl Acad Sci U S A.
1013 2016;113: E1738–E1746. doi:10.1073/pnas.1525528113

1014 41. Giles JA, Greenhalgh AD, Davies CL, Denes A, Shaw T, Coutts G, et al. Requirement for
1015 interleukin-1 to drive brain inflammation reveals tissue-specific mechanisms of innate
1016 immunity. Eur J Immunol. 2015;45: 525–530. doi:10.1002/eji.201444748

1017 42. Heneka MT, Kummer MP, Latz E. Innate immune activation in neurodegenerative
1018 disease. Nature Reviews Immunology. Nature Publishing Group; 2014. pp. 463–477.
1019 doi:10.1038/nri3705

1020 43. Allan SM, Tyrrell PJ, Rothwell NJ. Interleukin-1 and neuronal injury. Nature Reviews
1021 Immunology. Nat Rev Immunol; 2005. pp. 629–640. doi:10.1038/nri1664

1022 44. Nimmerjahn A, Kirchhoff F, Helmchen F. Neuroscience: Resting microglial cells are
1023 highly dynamic surveillants of brain parenchyma in vivo. Science (80-). 2005;308:
1024 1314–1318. doi:10.1126/science.1110647

1025 45. Davalos D, Grutzendler J, Yang G, Kim J V., Zuo Y, Jung S, et al. ATP mediates rapid
1026 microglial response to local brain injury in vivo. Nat Neurosci. 2005;8: 752–758.
1027 doi:10.1038/nn1472

1028 46. Fekete R, Cserép C, Lénárt N, Tóth K, Orsolits B, Martinecz B, et al. Microglia control
1029 the spread of neurotropic virus infection via P2Y12 signalling and recruit monocytes
1030 through P2Y12-independent mechanisms. Acta Neuropathol. 2018;136: 461–482.

1031 doi:10.1007/s00401-018-1885-0

1032 47. Heindl S, Gesierich B, Benakis C, Llovera G, Duering M, Liesz A. Automated
1033 morphological analysis of microglia after stroke. Front Cell Neurosci. 2018;12.
1034 doi:10.3389/fncel.2018.00106

1035 48. Kahle KT, Khanna AR, Alper SL, Adragna NC, Lauf PK, Sun D, et al. K-Cl cotransporters,
1036 cell volume homeostasis, and neurological disease. Trends in Molecular Medicine.
1037 Elsevier Ltd; 2015. pp. 513–523. doi:10.1016/j.molmed.2015.05.008

1038 49. Russell JM. Sodium-potassium-chloride cotransport. Physiological Reviews. American
1039 Physiological Society; 2000. pp. 211–276. doi:10.1152/physrev.2000.80.1.211

1040 50. Swanson K V., Deng M, Ting JPY. The NLRP3 inflammasome: molecular activation and
1041 regulation to therapeutics. Nature Reviews Immunology. Nature Publishing Group;
1042 2019. pp. 477–489. doi:10.1038/s41577-019-0165-0

1043 51. Heneka MT, McManus RM, Latz E. Inflammasome signalling in brain function and
1044 neurodegenerative disease. Nature Reviews Neuroscience. Nature Publishing Group;
1045 2018. pp. 610–621. doi:10.1038/s41583-018-0055-7

1046 52. Wendeln AC, Degenhardt K, Kaurani L, Gertig M, Ulas T, Jain G, et al. Innate immune
1047 memory in the brain shapes neurological disease hallmarks. Nature. 2018;556: 332–
1048 338. doi:10.1038/s41586-018-0023-4

1049 53. Eder C, Klee R, Heinemann U. Involvement of stretch-activated Cl- channels in
1050 ramification of murine microglia. J Neurosci. 1998;18: 7127–7137.
1051 doi:10.1523/jneurosci.18-18-07127.1998

1052 54. Ducharme G, Newell EW, Pinto C, Schlichter LC. Small-conductance Cl- channels
1053 contribute to volume regulation and phagocytosis in microglia. Eur J Neurosci.
1054 2007;26: 2119–2130. doi:10.1111/j.1460-9568.2007.05802.x

1055 55. Schlichter LC, Mertens T, Liu B. Swelling activated Cl- channels in microglia: Biophysics,
1056 pharmacology and role in glutamate release. Channels. 2011;5: 128–137.
1057 doi:10.4161/chan.5.2.14310

1058 56. Chen L, König B, Liu T, Pervaiz S, Razzaque YS, Stauber T. More than just a pressure
1059 relief valve: Physiological roles of volume-regulated LRRC8 anion channels. Biological
1060 Chemistry. De Gruyter; 2020. pp. 1481–1496. doi:10.1515/hsz-2019-0189

1061 57. Luo L, Song S, Ezenwukwa CC, Jalali S, Sun B, Sun D. Ion Channels and Transporters in
1062 Microglial Function in Physiology and Brain Diseases. Neurochem Int. 2020; 104925.
1063 doi:10.1016/j.neuint.2020.104925

1064 58. Izquierdo P, Attwell D, Madry C. Ion Channels and Receptors as Determinants of
1065 Microglial Function. Trends in Neurosciences. Elsevier Ltd; 2019. pp. 278–292.
1066 doi:10.1016/j.tins.2018.12.007

1067 59. Hung CM, Peng CK, Yang S Sen, Shui HA, Huang KL. WNK4–SPAK modulates
1068 lipopolysaccharide-induced macrophage activation. Biochem Pharmacol. 2020;171.
1069 doi:10.1016/j.bcp.2019.113738

1070 60. Lemonnier E, Degrez C, Phelep M, Tyzio R, Josse F, Grandgeorge M, et al. A
1071 randomised controlled trial of bumetanide in the treatment of autism in children.
1072 Transl Psychiatry. 2012;2: 202. doi:10.1038/tp.2012.124

1073 61. Javdani F, Hegedűs K, Miranda CO, Hegyi Z, Holló K, Antal M. Differential expression of
1074 Na+/K+/Cl− cotransporter 1 in neurons and glial cells within the superficial spinal
1075 dorsal horn of rodents. Sci Rep. 2020;10. doi:10.1038/s41598-020-68638-3

1076 62. Davalos D, Grutzendler J, Yang G, Kim J V, Zuo Y, Jung S, et al. ATP mediates rapid
1077 microglial response to local brain injury in vivo. Nat Neurosci. 2005;8: 752–758.
1078 doi:10.1038/nn1472

1079 63. Haynes SE, Hollopeter G, Yang G, Kurpius D, Dailey ME, Gan WB, et al. The P2Y12
1080 receptor regulates microglial activation by extracellular nucleotides. Nat Neurosci.
1081 2006;9: 1512–1519. doi:10.1038/nn1805

1082 64. Butovsky O, Jedrychowski MP, Moore CS, Cialic R, Lanser AJ, Gabriely G, et al.
1083 Identification of a unique TGF-β-dependent molecular and functional signature in
1084 microglia. Nat Neurosci. 2014;17: 131–143. doi:10.1038/nn.3599

1085 65. Schiapparelli P, Guerrero-Cazares H, Magaña-Maldonado R, Hamilla SM, Ganaha S,
1086 Goulin Lippi Fernandes E, et al. NKCC1 Regulates Migration Ability of Glioblastoma
1087 Cells by Modulation of Actin Dynamics and Interacting with Cofilin. EBioMedicine.
1088 2017;21: 94–103. doi:10.1016/j.ebiom.2017.06.020

1089 66. Ma H, Li T, Tao Z, Hai L, Tong L, Yi L, et al. NKCC1 promotes EMT-like process in GBM
1090 via RhoA and Rac1 signaling pathways. J Cell Physiol. 2019;234: 1630–1642.
1091 doi:10.1002/jcp.27033

1092 67. Madry C, Arancibia-Cárcamo IL, Kyrargyri V, Chan VTT, Hamilton NB, Attwell D. Effects
1093 of the ecto-ATPase apyrase on microglial ramification and surveillance reflect cell
1094 depolarization, not ATP depletion. Proc Natl Acad Sci U S A. 2018;115: E1608–E1617.
1095 doi:10.1073/pnas.1715354115

1096 68. Choi H, Rohrbough JC, Nguyen HN, Dikalova A, Lamb FS. Oxidant-resistant LRRC8A/C
1097 anion channels support superoxide production by NADPH oxidase 1. J Physiol.
1098 2021;599: 3013–3036. doi:10.1113/JP281577

1099 69. Brough D, Rothwell NJ, Allan SM. Interleukin-1 as a pharmacological target in acute
1100 brain injury. Experimental Physiology. Blackwell Publishing Ltd; 2015. pp. 1488–1494.
1101 doi:10.1113/EP085135

1102 70. Lambertsen KL, Biber K, Finsen B. Inflammatory cytokines in experimental and human
1103 stroke. Journal of Cerebral Blood Flow and Metabolism. J Cereb Blood Flow Metab;
1104 2012. pp. 1677–1698. doi:10.1038/jcbfm.2012.88

1105 71. Wofford KL, Loane DJ, Cullen DK. Acute drivers of neuroinflammation in traumatic
1106 brain injury. Neural Regeneration Research. Wolters Kluwer Medknow Publications;
1107 2019. pp. 1481–1489. doi:10.4103/1673-5374.255958

1108 72. Denes A, Thornton P, Rothwell NJ, Allan SM. Inflammation and brain injury: Acute
1109 cerebral ischaemia, peripheral and central inflammation. Brain, Behavior, and
1110 Immunity. Brain Behav Immun; 2010. pp. 708–723. doi:10.1016/j.bbi.2009.09.010

1111 73. Battey TWK, Karki M, Singhal AB, Wu O, Sadaghiani S, Campbell BCV, et al. Brain
1112 edema predicts outcome after nonlacunar ischemic stroke. Stroke. 2014;45: 3643–
1113 3648. doi:10.1161/STROKEAHA.114.006884

1114 74. Yao Y, Zhang Y, Liao X, Yang R, Lei Y, Luo J. Potential Therapies for Cerebral Edema

1115 After Ischemic Stroke: A Mini Review. Frontiers in Aging Neuroscience. Frontiers
1116 Media S.A.; 2021. doi:10.3389/fnagi.2020.618819

1117 75. Zhang J, Bhuiyan MIH, Zhang T, Karimy JK, Wu Z, Fiesler VM, et al. Modulation of brain
1118 cation-Cl− cotransport via the SPAK kinase inhibitor ZT-1a. Nat Commun. 2020;11:
1119 Zhang, J., Bhuiyan, M. I. H., Zhang, T., Karimy, J. doi:10.1038/s41467-019-13851-6

1120 76. Kilkenny C, Browne WJ, Cuthill IC, Emerson M, Altman DG. Improving Bioscience
1121 Research Reporting: The ARRIVE Guidelines for Reporting Animal Research. PLoS Biol.
1122 2010;8: e1000412. doi:10.1371/journal.pbio.1000412

1123 77. Percie du Sert N, Alfieri A, Allan SM, Carswell HVO, Deuchar GA, Farr TD, et al. The
1124 IMPROVE Guidelines (Ischaemia Models: Procedural Refinements Of in Vivo
1125 Experiments). Journal of Cerebral Blood Flow and Metabolism. SAGE Publications Ltd;
1126 2017. pp. 3488–3517. doi:10.1177/0271678X17709185

1127 78. Yona S, Kim K-W, Wolf Y, Mildner A, Varol D, Breker M, et al. Fate Mapping Reveals
1128 Origins and Dynamics of Monocytes and Tissue Macrophages under Homeostasis.
1129 Immunity. 2013;38: 79–91. doi:10.1016/j.immuni.2012.12.001

1130 79. Antoine MW, Hübner CA, Arezzo JC, Hébert JM. A causative link between inner ear
1131 defects and long-term striatal dysfunction. Science (80-). 2013;341: 1120–1123.
1132 doi:10.1126/science.1240405

1133 80. Donocoff RS, Teteloshvili N, Chung H, Shoulson R, Creusot RJ. Optimization of
1134 tamoxifen-induced Cre activity and its effect on immune cell populations. Sci Rep.
1135 2020;10. doi:10.1038/s41598-020-72179-0

1136 81. Otxoa-de-Amezaga A, Miró-Mur F, Pedragosa J, Gallizioli M, Justicia C, Gaja-Capdevila
1137 N, et al. Microglial cell loss after ischemic stroke favors brain neutrophil accumulation.
1138 Acta Neuropathol. 2019;137: 321–341. doi:10.1007/s00401-018-1954-4

1139 82. Giles JA, Greenhalgh AD, Denes A, Nieswandt B, Coutts G, McColl BW, et al.
1140 Neutrophil infiltration to the brain is platelet-dependent, and is reversed by blockade
1141 of platelet GPIbα. Immunology. 2018;154: 322–328. doi:10.1111/imm.12892

1142 83. Denes A, Coutts G, Lénárt N, Cruickshank SM, Pelegrin P, Skinner J, et al. AIM2 and
1143 NLRC4 inflammasomes contribute with ASC to acute brain injury independently of
1144 NLRP3. Proc Natl Acad Sci U S A. 2015;112: 4050–4055. doi:10.1073/pnas.1419090112

1145 84. McQuin C, Goodman A, Chernyshev V, Kamentsky L, Cimini BA, Karhohs KW, et al.
1146 CellProfiler 3.0: Next-generation image processing for biology. PLoS Biol. 2018;16.
1147 doi:10.1371/journal.pbio.2005970

1148 85. Dénes Á, Humphreys N, Lane TE, Grencis R, Rothwell N. Chronic systemic infection
1149 exacerbates ischemic brain damage via a CCL5 (regulated on activation, normal T-cell
1150 expressed and secreted)-mediated proinflammatory response in mice. J Neurosci.
1151 2010;30: 10086–10095. doi:10.1523/JNEUROSCI.1227-10.2010

1152 86. Bederson JB, Pitts LH, Tsuji M, Nishimura MC, Davis RL, Bartkowski H. Rat middle
1153 cerebral artery occlusion: Evaluation of the model and development of a neurologic
1154 examination. Stroke. 1986;17: 472–476. doi:10.1161/01.STR.17.3.472

1155 87. Iadecola C, Zhang F, Casey R, Nagayama M, Elizabeth Ross M. Delayed reduction of
1156 ischemic brain injury and neurological deficits in mice lacking the inducible nitric oxide

1157 synthase gene. J Neurosci. 1997;17: 9157–9164. doi:10.1523/jneurosci.17-23-
1158 09157.1997

1159 88. Schaar KL, Brenneman MM, Savitz SI. Functional assessments in the rodent stroke
1160 model. Experimental and Translational Stroke Medicine. Exp Transl Stroke Med; 2010.
1161 doi:10.1186/2040-7378-2-13

1162 89. Orsini F, Villa P, Parrella S, Zangari R, Zanier ER, Gesuete R, et al. Targeting mannose-
1163 binding lectin confers long-lasting protection with a surprisingly wide therapeutic
1164 window in cerebral ischemia. Circulation. 2012;126: 1484–1494.
1165 doi:10.1161/CIRCULATIONAHA.112.103051

1166 90. McColl BW, Rothwell NJ, Allan SM. Systemic inflammatory stimulus potentiates the
1167 acute phase and CXC chemokine responses to experimental stroke and exacerbates
1168 brain damage via interleukin-1- and neutrophil-dependent mechanisms. J Neurosci.
1169 2007;27: 4403–4412. doi:10.1523/JNEUROSCI.5376-06.2007

1170